Scientific Research Publishing

Open Journal of Geology, 2025, 15(12), 1029-1060
https://www.scirp.org/journal/ojg
ISSN Online: 2161-7589
ISSN Print: 2161-7570

Incorporation of Geospatial Data and Multi-Criteria Analysis for Mapping and Assessing the Mineral Potential of the Baïbokoum Pluton (Southern Chad)

Ronang Gustave Baïssemia[1*], Diondoh Mbaguedjé[2], Nenadji Félix Djerossem[3], Ousmanou Safianou[4], Nourene Souleymane Abdoulaye[1], Dedzo Merlin Gountié[5], Maurice Kwékam[6]

[1]Department of Mining and Geological Engineering, Faculty of Life and Earth Sciences, Pala University, Pala, Chad
[2]Department of Geology, Faculty of Sciences and Techniques, Adam Barka University of Abeché, Abéché, Chad
[3]Department of Mining, New and Renewable Energies, National Higher Institute of the Sahara and Sahel, Iriba, Chad
[4]Institute of Geological and Mining Research, Yaoundé, Cameroon
[5]Department of Life and Earth Sciences, High Teachers' Training College, University of Maroua, Maroua, Cameroon
[6]Department of Earth Science, Faculty of Science, University of Dschang, Dschang, Cameroon
Email: *baissemiarg@gmail.com

How to cite this paper: Baïssemia, R.G., Mbaguedjé, D., Djerossem, N.F., Safianou, O., Abdoulaye, N.S., Gountié, D.M. and Kwékam, M. (2025) Incorporation of Geospatial Data and Multi-Criteria Analysis for Mapping and Assessing the Mineral Potential of the Baïbokoum Pluton (Southern Chad). *Open Journal of Geology*, **15**, 1029-1060.
https://doi.org/10.4236/ojg.2025.1512054

Received: October 27, 2025
Accepted: December 21, 2025
Published: December 24, 2025

Abstract

The Baïbokoum area offers significant potential for geological and mining exploration. However, the region is not well known due to insufficient studies on mineral and rock mapping, as well as other indicators of mineralization. In this study, we examine lithological units and potential hydrothermal alteration zones in the Baïbokoum region using remote sensing, geographic information systems (GIS), and statistical analysis, which are essential tools for geological exploration. Landsat 9 OLI data, combined with the main techniques used (e.g. FCC, BR, MNF, PCA, SEM, SAM), and field observations, are used to identify rock units and potential mineralization. Using a variety of techniques, we were able to identify orthogneisses, granites, and basalts rich in iron oxides, hydroxyl, and ferrous metals that could constitute potential mineral deposits in the Baïbokoum area. Statistical examination of the geochemical data indicates that the Baïbokoum syenites, which are calcic, alkaline-calcic, and slightly peraluminous, demonstrate that their original magma was rich in mineralization for major elements and rare earth elements, Al_2O_3, Fe_2O_3, MgO, CaO, Na_2O, MnO, P_2O_5, V, Cr, W, Zr, Nb, Cs, Ba, Y, Hf, Ta, Th, U, and REE. In addition, the study of lineaments revealed three structural orientations in the area (NE-SW, E-W, NNE-SSW, and NW-SE). This study is innovative in

that it integrates and processes Landsat 9 OLI and performs statistical geochemical analysis of previous data, and conducts field investigations. These actions make it possible to identify rock units and potentially mineralized formations, as well as to determine exploration targets.

Keywords

Landsat 9 OLI, Statistical Analyses, Mineralization Potential, Baïbokoum Region, Southern Chad

1. Introduction

Rocks contain a limited set of minerals defined by a distinct origin [1]. According to [2], affected zones in plutonic rocks are regions where a dynamic mineralogical chemical reaction occurs due to the passage of hydrothermal solutions, as well as zones of weakness and fractures present in the bedrock. Hydrothermally affected rocks have attracted considerable interest due to their potential economic benefits and spectral characteristics conducive to remote sensing [1] [3]. Thus, remote sensing and statistical analysis are effective in geological investigations, given the need to detect positive or negative anomalies as well as spatial signals for lithological and mineral mapping [1] [4]-[8]. The lack of geological, cartographic (based on Landsat data), and metallogenic data is the reason behind the choice of the Baïbokoum pluton. Recent studies by [9]-[11] have described the geochemistry of magmatic and metamorphic rocks (gneiss, syenite, amphibolite, and diorite). With this in mind, the use of satellite imagery could enable several new potential areas to be targeted before undertaking detailed and costly exploration work in the field [12]-[16]. These techniques have provided practical tools for describing and recognizing geological units, structures, and rock features, which have been combined with statistical data to locate areas of mineralization [17]-[19]. Thanks to their high spatial, spectral, and radiometric accuracy, remote sensing instruments are invaluable in the search for mineral deposits, particularly for detecting mineral-rich regions [1] [15] [20]-[25].

Over the past three decades, a large number of researchers have exploited multispectral data from satellites [3] [14] [16] [22] [26] [27] and statistical analysis of geochemical data [4] [6] [28] to locate mineralized areas. Across the globe, various exploratory methods have been implemented in research aimed at mapping and assessing the mineralization potential of granitic masses. These methods range from conventional techniques (mineralogy, thermobarometry, geochemical mapping, and structural analysis) to advanced techniques such as geophysics [18] [29]; remote sensing [14] [16] [23] [27] [30], geochemical data statistics [4] [6] [8] [28] [31].

In addition, these analysis methods include the use of false color (FCC), spectral ratio (BR), standard and selective principal component analysis (PCA), and spectral angle classifier (SAM). The use of techniques based on geographic infor-

mation systems, such as fuzzy logic, to develop mining prospecting maps from satellite data has proven to be an effective and accurate tool for identifying target areas for mining exploration [12] [14] [16] [19] [32], particularly during the investigation phase.

For example, fuzzy logic has been successfully used to map and identify gold mineralization in north-central Nigeria [16] [27]. Furthermore, according to statistical analysis of geochemical data, granitic rocks contain significant amounts of essential metals [33] [34], including Fe, Cu, Au, Ag, Zn, Ga, and Mo, which are commonly found in Type I granites, as well as Sn and W, which are found in Type S granites [35]. In the modern technology sector, these metals are widely used due to their specific characteristics in electronics, magnetism, optics, and catalysis.

In Chad, syenites or type I and S granites are widely distributed, and previous studies conducted on these rocks in the Mayo Kebbi region to determine and map the concentration of the aforementioned strategic metals, including, for example, the work of [36] or [37], highlight the potential for mineralization in Sn, Fe, Zr, Au, U, rutile, and pyrite. In eastern Chad, the work of [38] in the Goz-Béïda area has highlighted gold mineralization in quartz veins, which have a NW-SE to NE-SW or ENE-WSW to NE-SW direction.

All these authors have adopted either traditional methods (such as field surveys) or modern methods (such as geochemical data analysis). To date, no studies have been conducted in this region or in Chad in general. As a result, the combined approach of several methods used by some authors in the neighboring country (such as [4] [24] and [28]; geospatial and statistical), which could clearly and easily highlight the mineralization potential, has never been tested. This situation leads to a gap in the updating of the mining map. This article uses a combination of geospatial data (Landsat 9 OLI data and the Fuzzy method) and statistical analysis of geochemical data to map and evaluate the mineralization of a plutonic body. The case study is the Baïbokoum pluton, located in the Adamaoua-Yadé domain in Chad.

2. Geological Setting

2.1. Pan-African Belt in Chad

Located on the border of the Adamawa-Yadé shear zone, Chad is part of the Central Pan-African Belt (CPAB) (**Figure 1(a)** and **Figure 1(b)**; [44] [49]). The Oubanguides [50] are referred to as the CPAB, which is located north of the Congo craton. This belt extends across Chad, Cameroon, and the Central African Republic, continuing on to Sudan. The development of the CPAB is seen as a point of convergence and collision between the São Francisco-Congo cratons, the West African craton (WAC) and the Sahara metacraton as defined by [44] [49] Abdelsalam *et al.* (2002), Toteu *et al.* (2004) and [51]. In Chad, the CPAB extends over the Baïbokoum massif in the south, the Ouaddaï in the east, the Tibesti massifs in the north, the Mayo Kebbi massif in the southwest, and the Guéra massif in the center. According to [52], the Tibesti is composed of metasediments, metavolcanics,

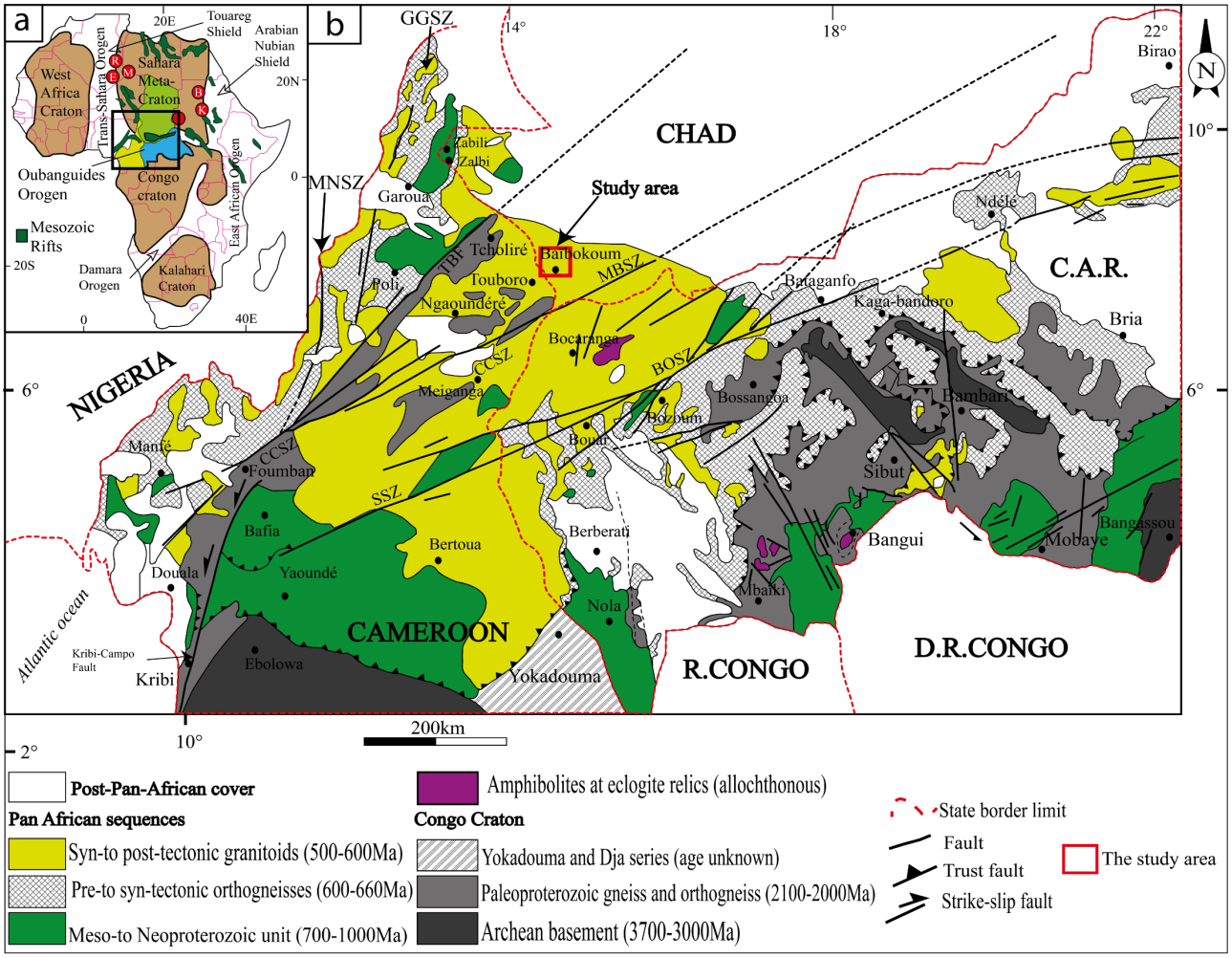

Figure 1. (a) Map of Africa showing the different orogens, craton and central African mobile zone (after [39] [40]; (b) Geological map of Central Africa (after [41]-[48]) showing the main litho-tectonic units and domains of the Central African Orogenic Belt (SZ—Shear Zone; CCSZ—Central Cameroon shear zone; MNSZ—Mayo Nolti shear zone; SSZ—Sanaga shear zone; MBSZ—M'Béré shear zone; BOSZ—Bozoum-Ndélé shear zone; TBF—Tcholliré Banyo fault; CAR—Central African Republic; R. Congo—Republic of Congo; D.R. Congo—Democratic Republic of the Congo.

and a variety of amphibolites, with local occurrences of migmatites in enclaves and lenses within gneisses and granitoids. The Tibesti massif has been dated to between 1250 and 820 million years old using Rb-Sr techniques on whole rocks, as mentioned by [53] and [54]. The Ouaddaï massif consists of metasedimentary series crossed by huge peraluminous leucogranitic batholiths and small plutons of pyroxene monzonite, hornblende monzogabbro, and biotite granite, giving rise to a strongly potassic to shoshonitic calc-alkaline series [55]-[57]. U-Pb dating on zircon has determined that the age of the peraluminous granites is 635 ± 3 Ma [57] for biotite leucogranites, while it is 613 ± 8 Ma for muscovite and garnet leucogranites [57]. The age of the metaluminous, calc-alkaline, and strongly potassium-rich to shoshonitic series has been given as 540 ± 5 Ma in biotite granites, as shown by [57]-[60] in their studies on the U-Pb of zircons. The Baïbokoum massif, which extends to the southern border of Chad and continues into the Central

African Republic and Cameroon, represents an extension of the Adamwa-Yadé territory. The Baïbokoum massif, which extends along the southern border of Chad and continues into the Central African Republic and Cameroon, represents an extension of the Adamwa-Yadé territory. The Baïbokoum massif has been little explored, with only general aspects having been identified in the research of Jérémie and [9]-[11] [58] [61]-[64]). Several rocks in the massif date from the Neoproterozoic, including syenites (654 Ma, determined by the K-Ar method on whole rock), as well as granites and a syenite (632 and 568 Ma, established by K-Ar and Rb-Sr on whole rock [65] [58]). The Mayo-Kébbi Massif is a structure extending in a northeast-southwest direction between the extensions of the Tcholliré faults in Chad. It is distinguished by its juvenile Neoproterozoic crust [66]-[69]. This region represents a magmatic arc zone that formed between 800 Ma and 550 Ma following successive collisions with the Central Cameroon and North Cameroon domains, respectively [66]-[68]. It encompasses the greenstone belt, the batholith, and post-tectonic intrusions [36] [55] [66]-[68] [70]. The Guéra massif, which has around ten charnockitic formations ranging from noritic to granitic in composition, with a predominance of syenite [71] [72], as well as small massifs with gabbroic and granodioritic compositions, often oriented and present as enclaves in heterogeneous granite, could be evidence of the oldest rocks in the Massif Central [71] [73].

2.2. Geology of the Baïbokoum Region

Baïbokoum is located in the Adamawa-Yadé zone, also known as the Central Cameroon Shear Zone or the Adamawa Shear Zone ([74]; **Figure 1(b)**). Vast areas of Paleoproterozoic metasedimentary rocks and orthogneisses ([44] [75]) outcrop in the Yadé massif. Based on Sm-Nd model ages and inherited zircon ages, [44] proposed that the metasediments and orthogneisses of the Adamawa-Yadé territory show significant influence from the Archean crust, comparable to that of the Congo craton [48]. Initial geological work carried out by [9]-[11] [65] [66] identified the following in the Baïbokoum area: (i) syenites; (ii) monzonites; (iii) hornblende-biotite orthogneisses; (iv) biotite gneisses and syenodiorites (**Figure 2**).

3. Materials and Methods

3.1. Data and Pre-Processing

In this study, the equipment and methods used and monitored in the Baïbokoum area are illustrated in the following flow chart (**Figure 3**). Landsat 9 OLI bands (LC09_L1TP_183055_20250218_20250218_02_T1) obtained on February 18, 2025, and downloaded from USGS site web (https://doi.org/10.5066/P975CC9B), cloud cover 0.21. Geodetic parameters (Map projection = "utm", datum = "wgs84", ellipsoid = "wgs84", utm zone = 33). Landsat 9 OLI data consist of a collection of nine bands (bands 1-9) and two TIR (thermal infrared) bands (bands 10-11). In this work, the Landsat 9 OLI bands visible and near infrared (VNIR), shortwave infrared (SWIR) and panchromatic (b8) bands were used. Principal

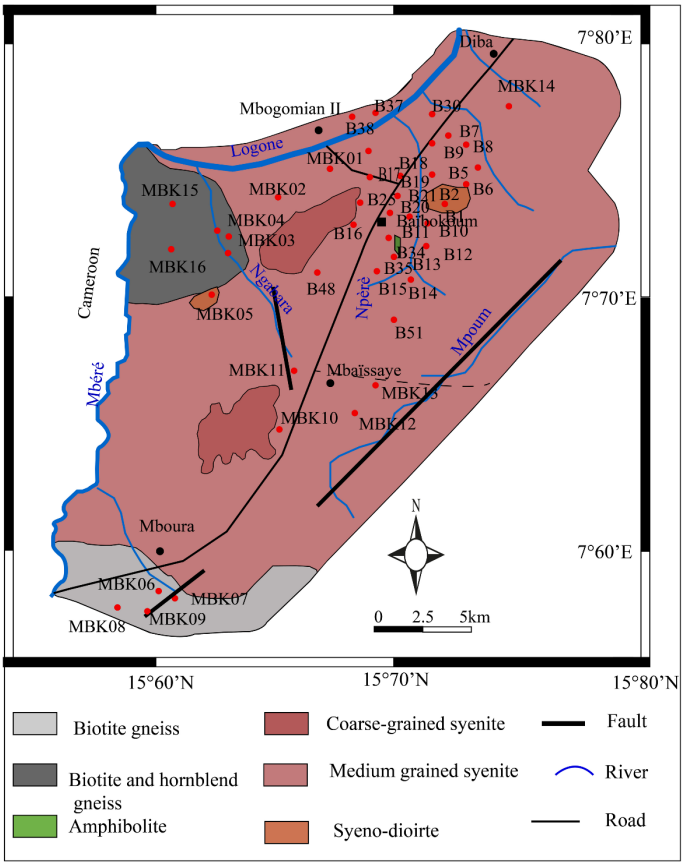

Figure 2. Geological sketch map of the study area showing sample station.

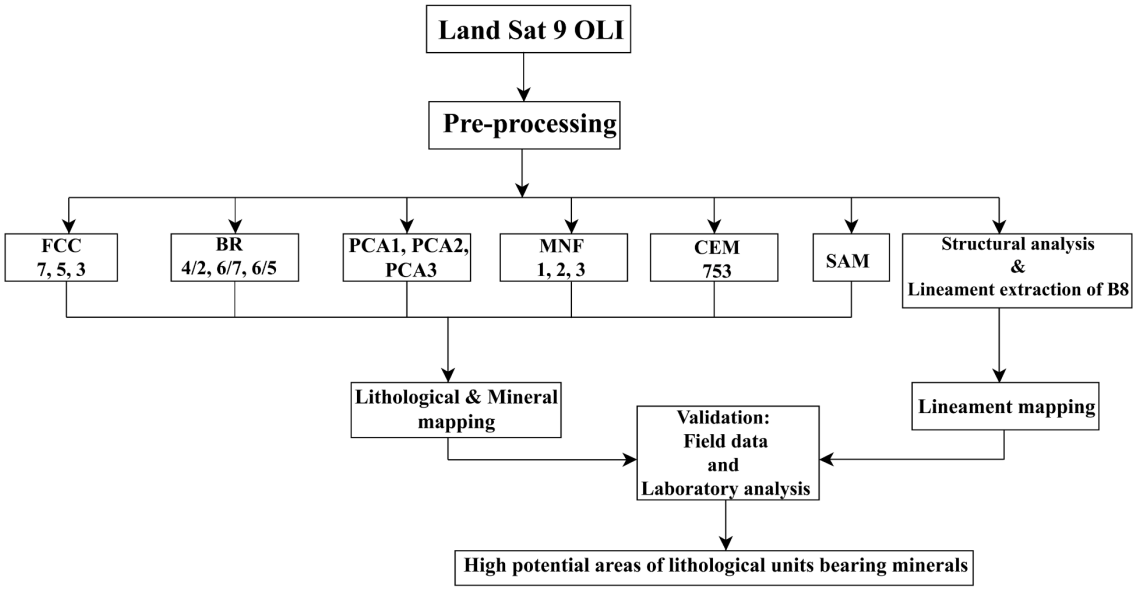

Figure 3. Methodological flowchart.

component analysis (PCA) was applied to the spectral bands of Landsat-9 data to highlight the exposed rock units of the study area using petrography.

Envi 5.3 software was used to apply radiometric correction to Landsat 9 OLI

bands. Radiometric calibrations and fast atmospheric corrections (QUAC) were applied to the Landsat 9 VNIR-SWIR bands for high-precision detection. Indeed, QUAC performs atmospheric correction better than other methods such as Fast Line-of-sight Atmospheric Analysis of Spectral Hypercube (FLAASH), generally producing a reflectance spectrum that is between 10% and 15% of the ground truth [76]. In addition, lineaments were extracted using PCI software version 9.1 with two different datasets, namely the high-resolution digital model. The rosette and lineament statistics were obtained from RockWorks software and finally the layout was done with ArcGIS 10.8 software. field campaigns collected samples on different lithological types and in the laboratory thin section making and description were carried out.

3.2. Geochemical Data and Statistical Analysis

The geochemical data (major elements, trace elements, and rare earth elements) used in this study were obtained from [9] and analyzed for whole rock chemistry at the laboratories of ALS Chemex South Africa (Pty), Ltd. in Johannesburg, South Africa. Major element analysis was performed by inductively coupled plasma atomic emission spectrometry (ICP-AES); 0.2 g of rock powder was fused with 1.5 g of LiBO2 and then dissolved in 100 mm of 35% HNO3. Trace and rare earth element content was determined by ICP-MS from pastes after dissolving 0.25 g of rock powder using four acid digests. Analytical precisions range from 0.1% to 0.02% for major elements, 0.01 to 0.5 ppm for trace elements, and 0.01 to 5 ppm for rare earth elements.

These geochemical data were plotted on discrimination diagrams to determine the productivity of each sample in certain strategic metals, as is generally recommended in granitoid metallogeny [35] [77]-[79]. In addition, the geochemical data were statistically processed using the GeoChemical Data toolkit (GCDkit.6.0; [80]) supported by R.3.6.0 software (for Windows) to identify positive or negative anomalies in the data. The normal distribution of the selected metals was tested using histograms and box plots in accordance with [81]. In the box plots, the bold line in the middle of the boxes is the median or 50^{th} percentile, and is given such that Q2 = 50%. The first quartile Q1 and third quartile Q3 (25%) and (75%) are the lower percentile and upper percentile, respectively. However, the difference between Q1 and Q3 is known as the interquartile range (IQR), where IQR indicates the extreme values calculated from a window of 1.5 * IQR. The statistical threshold for element concentration was calculated using the following formula: Threshold = Q3 + 1.5 * (IQR) for the upper threshold [81]), with IQR = Q3 − Q1. Values above or below the threshold are outliers and represent positive and negative anomalies, respectively.

4. Results

A combination of image processing techniques was applied to Landsat 9 OLI data to enhance lithological and mineralogical mapping in a Precambrian terrain. Each

method provided unique insights into the spectral behaviour of surface materials, contributing to a more reliable geological interpretation.

4.1. False Colour Composite (FCC)

FCCs using combinations like (Band 7, 5, 3) visually enhanced differences between vegetation, soil, and rock types. Igneous terrains (syenites) appeared in light pink tones, while metamorphic (gneiss) and sedimentary (shale) rock units showed green and white hues respectively (Figure 4). Also, the study area river display blue hues. FCCs offered a qualitative but quick overview for initial lithological discrimination (Figure 4).

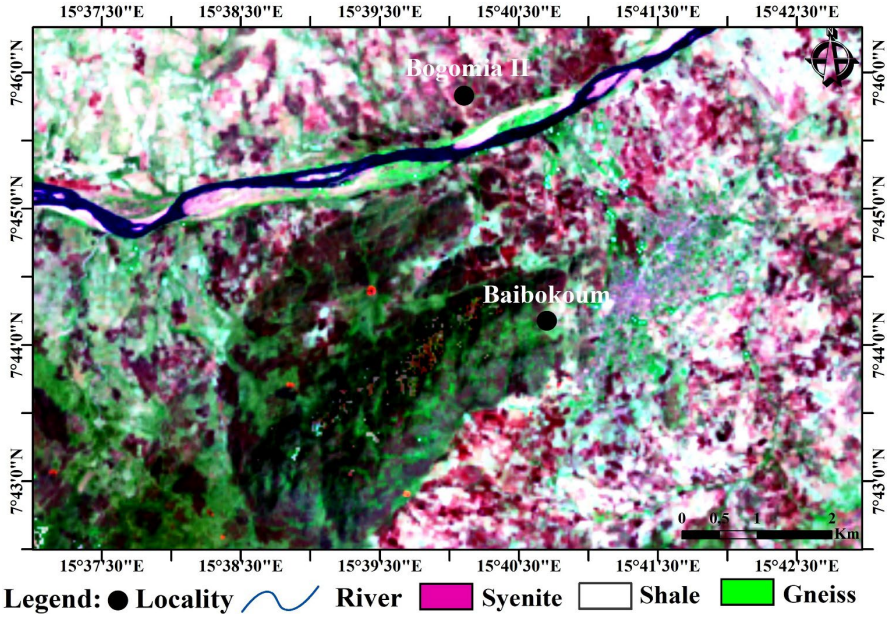

Figure 4. FCC of Baïbokoum area.

4.2. Principal Component Analysis (PCA)

PC1 and PC2 accounted for broad lithological variation. PC3 isolated specific spectral anomalies linked to mineralized zones. PCA maps (Figure 5) revealed rock units as syenites (in cyan tone), gneisses (in orange tone), and shales (in yellow tone) and contacts not easily detected in raw bands or FCCs.

According to Table 1 analysis of the eigenvector and eigenvalue loadings derived from PCA analysis of the Landsat 9 OLI bands (B2, 3, 4, 5, 6, and 7), PC1, PC2 and PC3 comprises a satisfactory loading from each of the 06 PC bands and makes up 92.86%, 5.94% and 0.84% respectively of the total data. It is therefore perfect for focusing on geological formations.

4.3. Minimum Noise Fraction (MNF)

The detection of rock types and alteration regions was done using the MNF1, 2, and 3 of OLI bands that were derived using MNF analysis. Syenites are identified as yellow to light-green hues, gneisses as pink, and shale as blue coloration in the

resulting MNF pictures, which have been subjected to an RGB composite analysis (Figure 6).

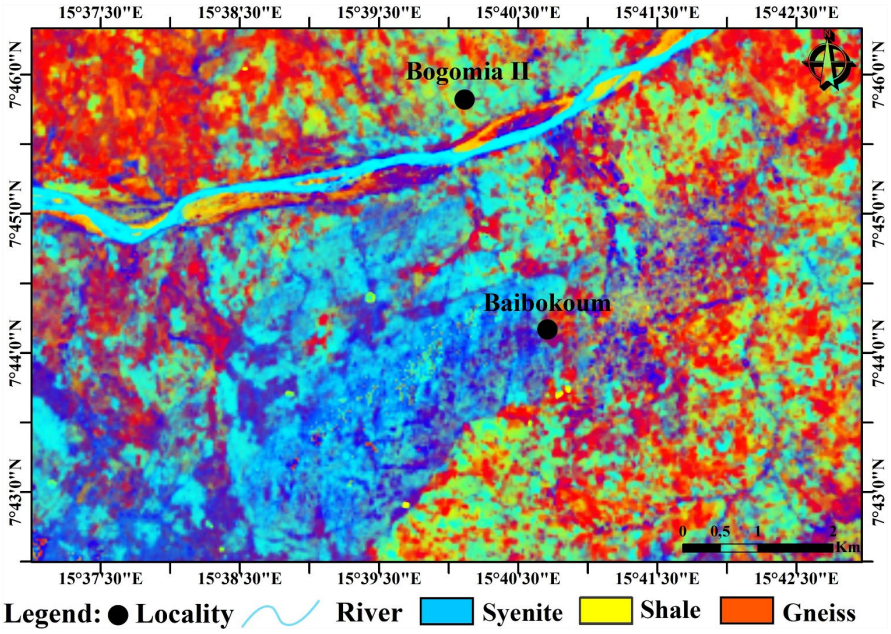

Figure 5. PCA map of Baïbokoum.

Table 1. PC values of OLI bands 2, 3, 4, 5, 6 and 7.

Eigenvector	Band 2	Band 3	Band 4	Band 5	Band 6	Band 7	Eigenvalue	Variance %
PC 1	−0.783	0.125	0.594	−0.078	−0.064	0.088	6,866,890.55	92.86
PC 2	−0.047	0.936	−0.289	−0.022	−0.190	0.036	439,060.8	5.94
PC 3	−0.333	0.044	−0.251	0.618	0.537	−0.392	62,266.55	0.84
PC 4	−0.502	−0.256	−0.679	−0.467	−0.045	0.034	24,774.32	0.34
PC 5	0.146	0.191	0.191	−0.626	0.613	−0.371	1354.07	0.02
PC 6	0.014	0.062	−0.055	0.041	0.542	0.835	608.33	0.01

According to Table 2 analysis of the eigenvectors and eigenvalues loadings derived from MNF analysis of the Landsat 9 OLI bands (B1, 2, 3, 4, 5, 6, and 7), MNF1, MNF2 and MNF3 comprises a satisfactory loading from each of the 07 MNF bands and makes up 12.89%, 9.08% and 6.12% respectively of the total data. It is therefore perfect for focusing on geological formations.

4.4. Band Ratios (BR)

Band ratios such as (4/2), (6/7), and (6/5) were particularly useful for: Highlighting the study area lithological units (syenites, gneisses and shales), iron oxide (e.g., hematite/goethite, Figure 7(a)), ferrous (Figure 7(b)), clay minerals (Figure 7(c)) and hydrothermal alteration zones (Figure 7(d)). Syenites display purple tones, shales exhibit pink tones while gneisses are distinguished by light green

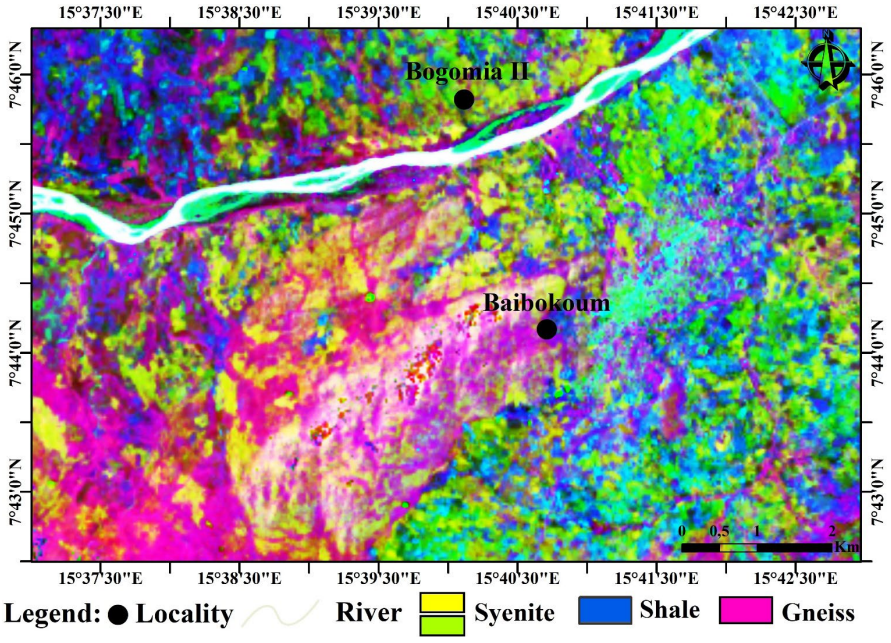

Figure 6. MNF map of Baïbokoum.

Table 2. MNF values of OLI bands 1, 2, 3, 4, 5, 6 and 7.

Eigenvector	Band 1	Band 2	Band 3	Band 4	Band 5	Band 6	Band 7	Eigenvalue (%)
MNF1	−1.00	0.00	0.00	0.00	0.00	0.00	0.00	12.89
MNF2	−0.00	−1.00	0.00	−0.00	0.00	−0.00	−0.00	9.08
MNF3	0.00	0.00	1.00	0.00	0.00	−0.00	0.00	6.12
MNF4	0.00	−0.00	−0.00	1.00	0.00	−0.00	0.00	4.73
MNF5	−0.00	−0.00	0.00	0.00	−1.00	−0.00	−0.00	3.61
MNF6	−0.00	0.00	−0.00	−0.00	0.00	−1.00	−0.00	1.92
MNF7	−0.00	0.00	0.00	0.00	0.00	0.00	−1.00	1.41

and yellow (Figure 7(d)).

4.5. Constrained Energy Minimization (CEM)

We used the USGS laboratory mineral spectra's (biotite, chlorite, goethite, hematite, illite, ilmenite, kaolinite, magnetite, pyrite and rutile) to run the CEM algorithm on 753 OLI band because of their spectral properties (Figure 8). Hence, the minerals in the study area shows up several tones (Figure 8).

4.6. Spectral Angle Mapper (SAM)

Using endmembers extracted from known mineral spectra (e.g., USGS library; Figure 9(a)), SAM accurately identified rocks such as syenite, shale and gneiss (Figure 9(b)) based on a fixed threshold (*i.e.* angle radian = 0.1). The syenitic, gneissic and shale rocks exhibit green, red and light-blue pixels (Figure 9(b)).

Therefore, following multiple tests, the accuracy evaluation findings (Table 3) of the SAM classification utilizing the confusion matrix methodology showed that the classification method overall accuracy is 100% with a Kappa coefficient of 1.00.

4.7. Lineament Analysis

Figure 10(a) and Figure 10(b), which reveal that each rock unit retains its lineament

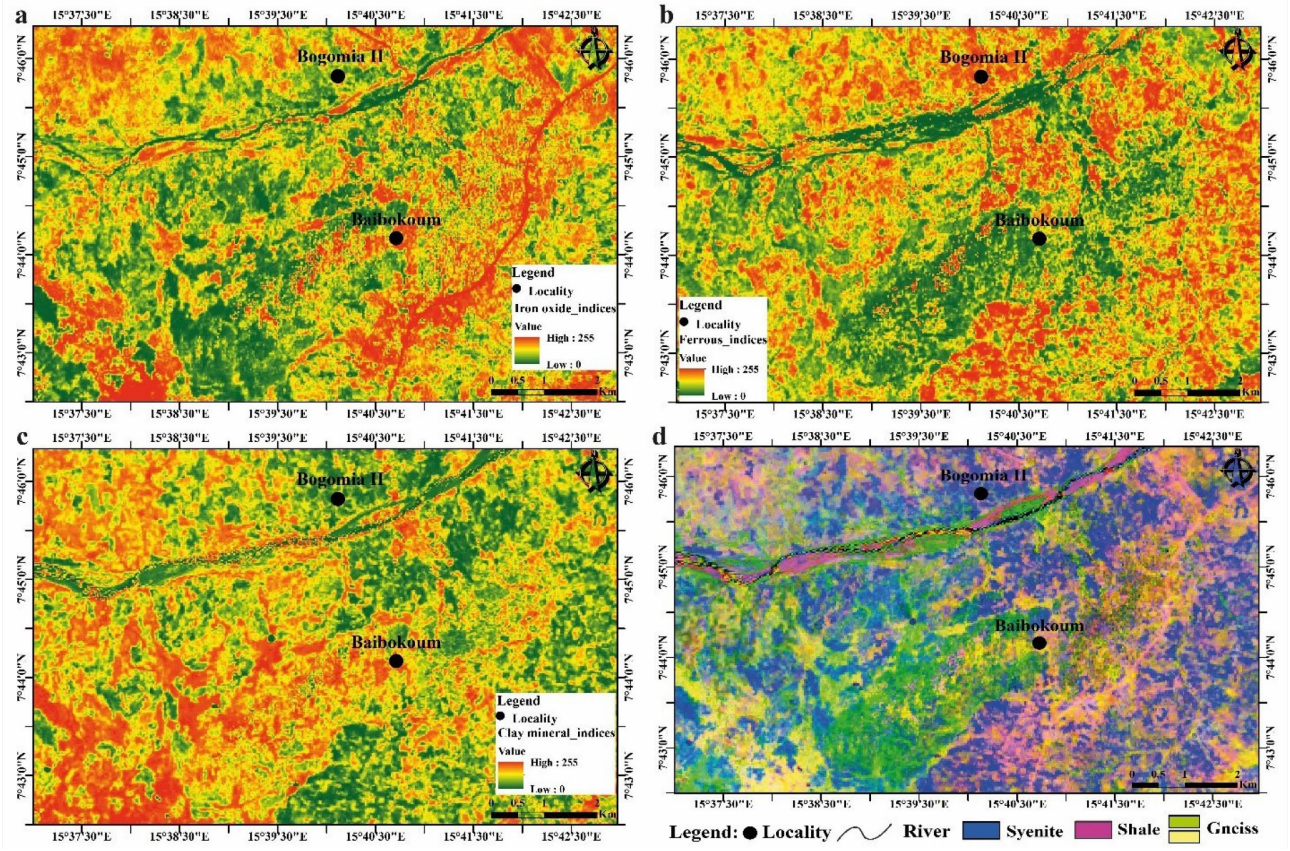

Figure 7. PCA map of Baïbokoum.

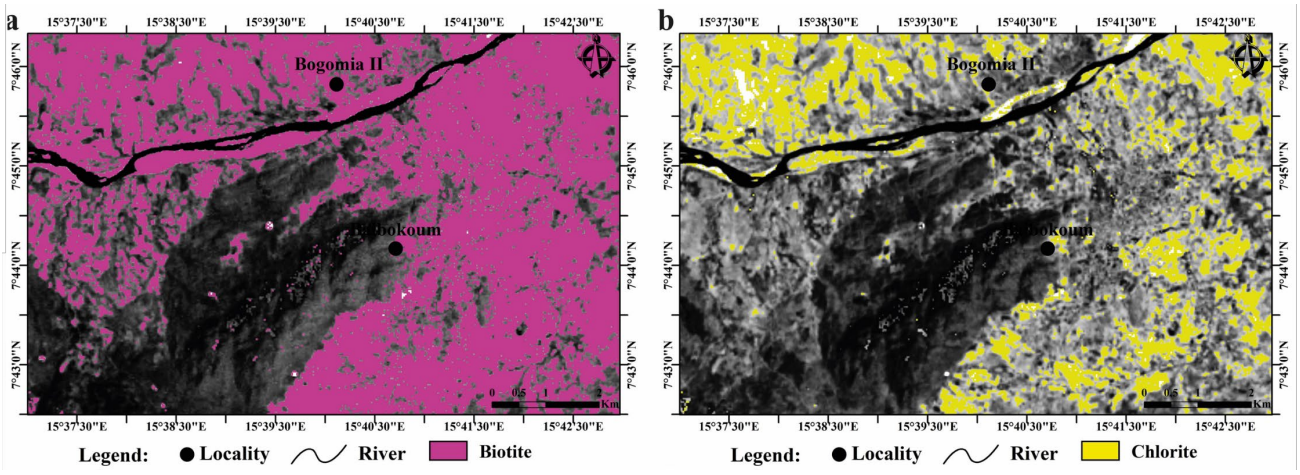

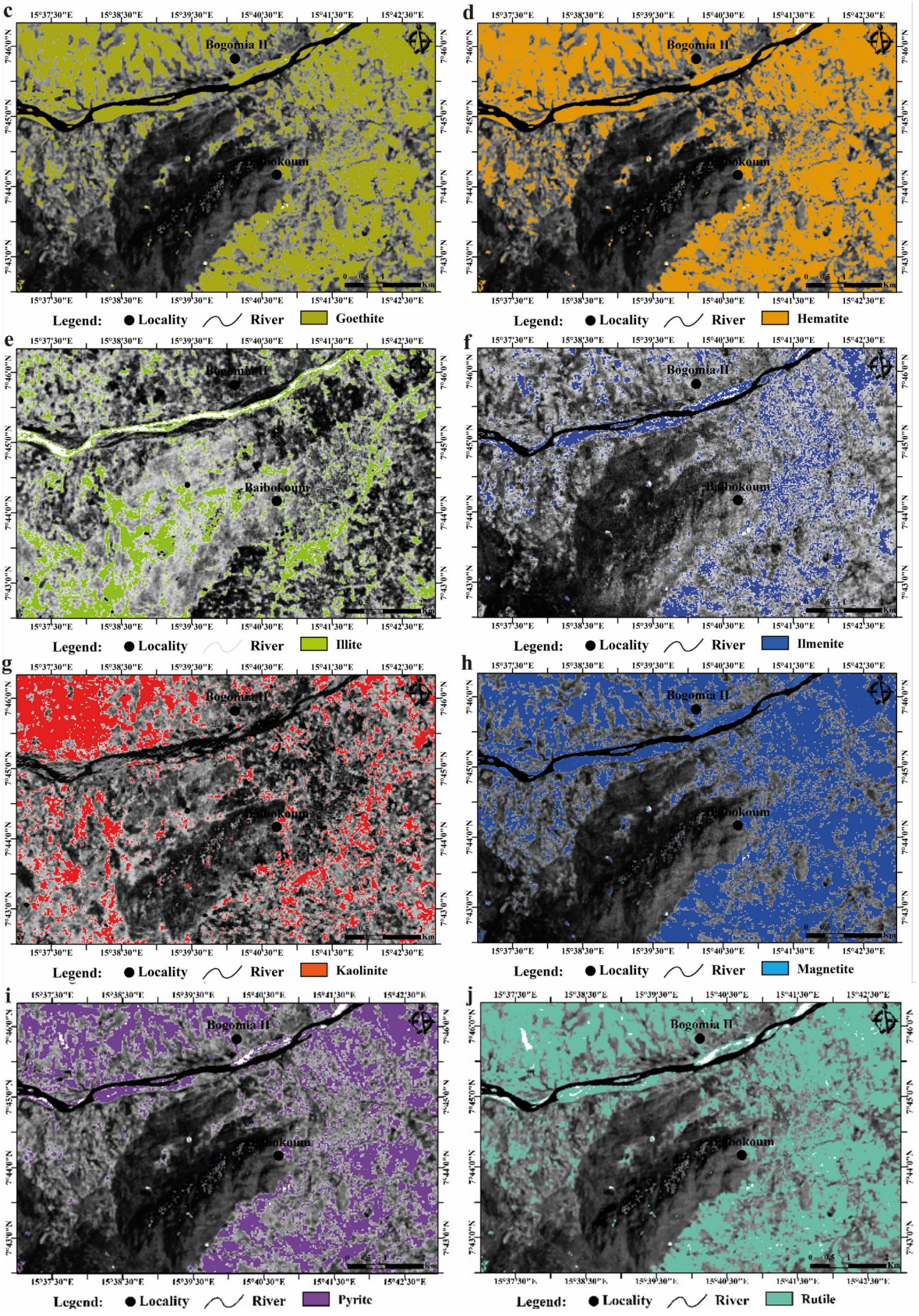

Figure 8. CEM map of Baïbokoum.

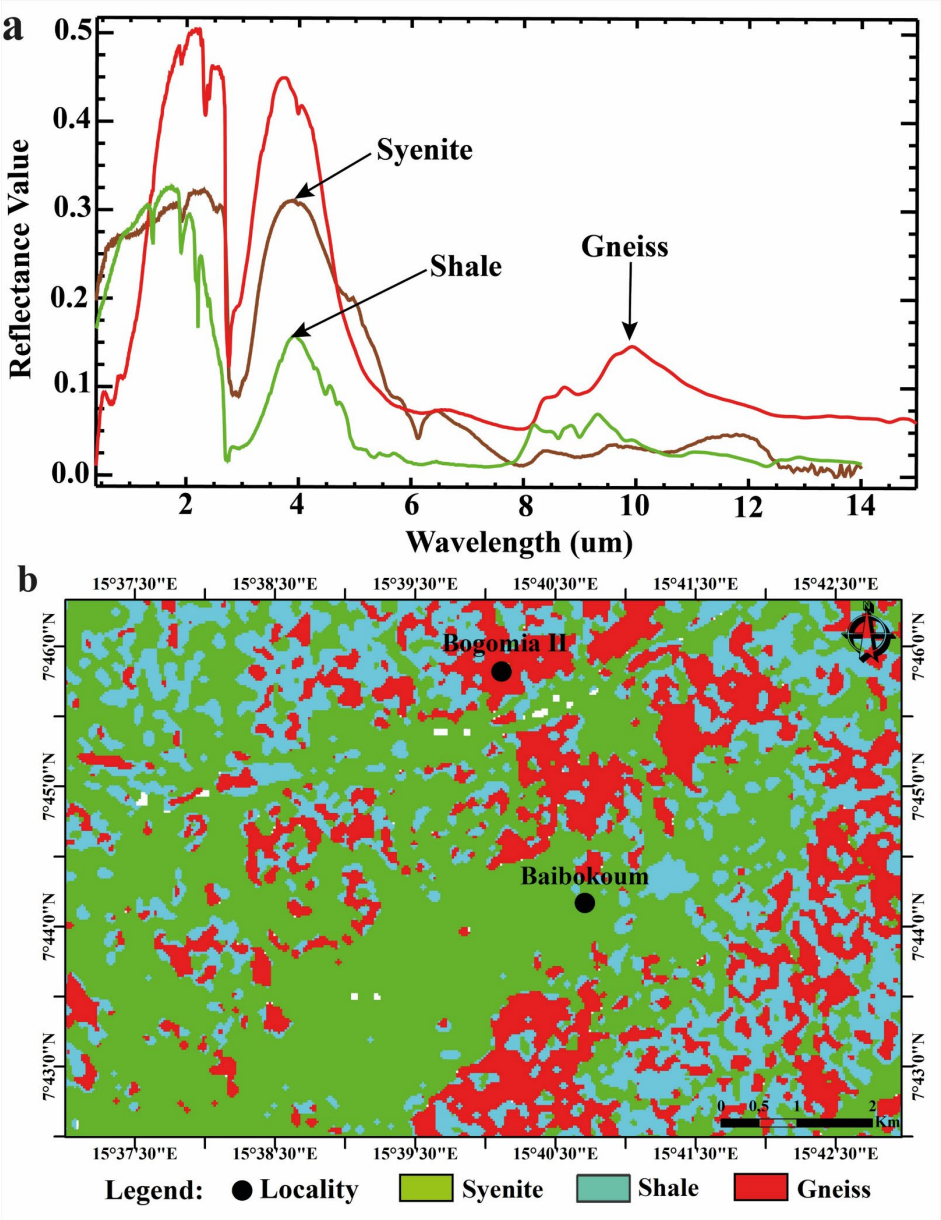

Figure 9. SAM classification map of Baïbokoum.

Table 3. Confusion matrix values.

Class	Shale	Diorite	Syenite	Total	Production Accuracy (%)	User Accuracy (%)
Shale	100	0	0	25.44	100	100
Diorite	0	100	0	22.97	100	100
Syenite	0	0	100	51.58	100	100
Total (%)	100	100	100	100		
OA (%)	100					
Kappa	1.00					

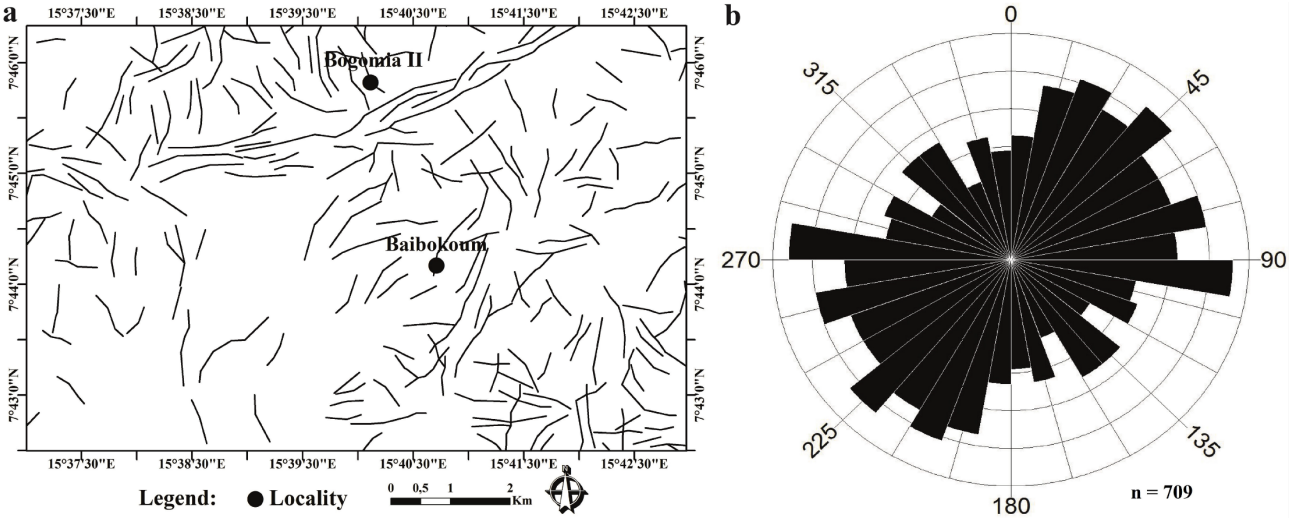

Figure 10. Lineament map of Baïbokoum area with rose diagram.

trend according to the created lineament map (**Figure 10(a)**), are the findings of lineament studies (manual and automated extraction) within the Baïbokoum area by processing band 8 (panchromatic band) of Landsat 9 OLI data. Two primary trends were discovered by the rose diagram of the lineaments: a NE-SW trend and E-W trend. Additionally, an extra NNE-SSW trend is noted (**Figure 10(b)**).

5. The Baïbokoum Pluton and Petrography

The Baïbokoum region is located between the Adamawa-Yade domain [44] and the Tcholliré-Banyo shear zone ([45]; **Figure 1(b)** and **Figure 2**), at longitudes 15˚60'E-15˚80'E and latitudes 7˚60'N -7˚80'N. The Baïbokoum pluton rests on syenites, Panafrican granitoids intruded into the orthogneiss basement ([9]-[11], **Figure 2**). In the area south and west of the study zone (**Figure 11**), the orthogneiss occurs in sheets and has a grano-porphyroblastic texture. It is striated and dark gray in color, with light quartzo-feldspathic bands alternating with darker biotite-hornblende bands (**Figure 11(a)**). In the rocks, apatite, titanite, and opaques occur as accessory minerals (**Figure 11(b)**). However, in the study area, coarse- and medium-grained syenites outcrop in the form of slabs or bowls, some of which are crossed by pegmatite veins containing magnetite and tourmaline (**Figures 11(c)-(e)**) and exhibit a heterogeneous granular texture. The main minerals are K feldspars, plagioclase, biotite, and amphibole. Accessory phases include apatite and zircon (**Figures 11(d)-(f)**).

6. Classification of Mineral Potential

The concentration of selected elements of metallogenic interest, such as Al_2O_3, Fe_2O_3, MgO, CaO, Na_2O_3, MnO, P_2O_5, V, Cr, W, Zr, Nb, Cs, Ba, Y, Hf, Ta, Th, U, and REE, was compared to their Clarke values (**Table 4**). In the Fe_2O_3/FeO vs. FeOt diagram by [82], the syenites, microsyenodiorites, and syenodiorites of Baïbokoum occupy the "reduced" domain, which indicates that they belong to the

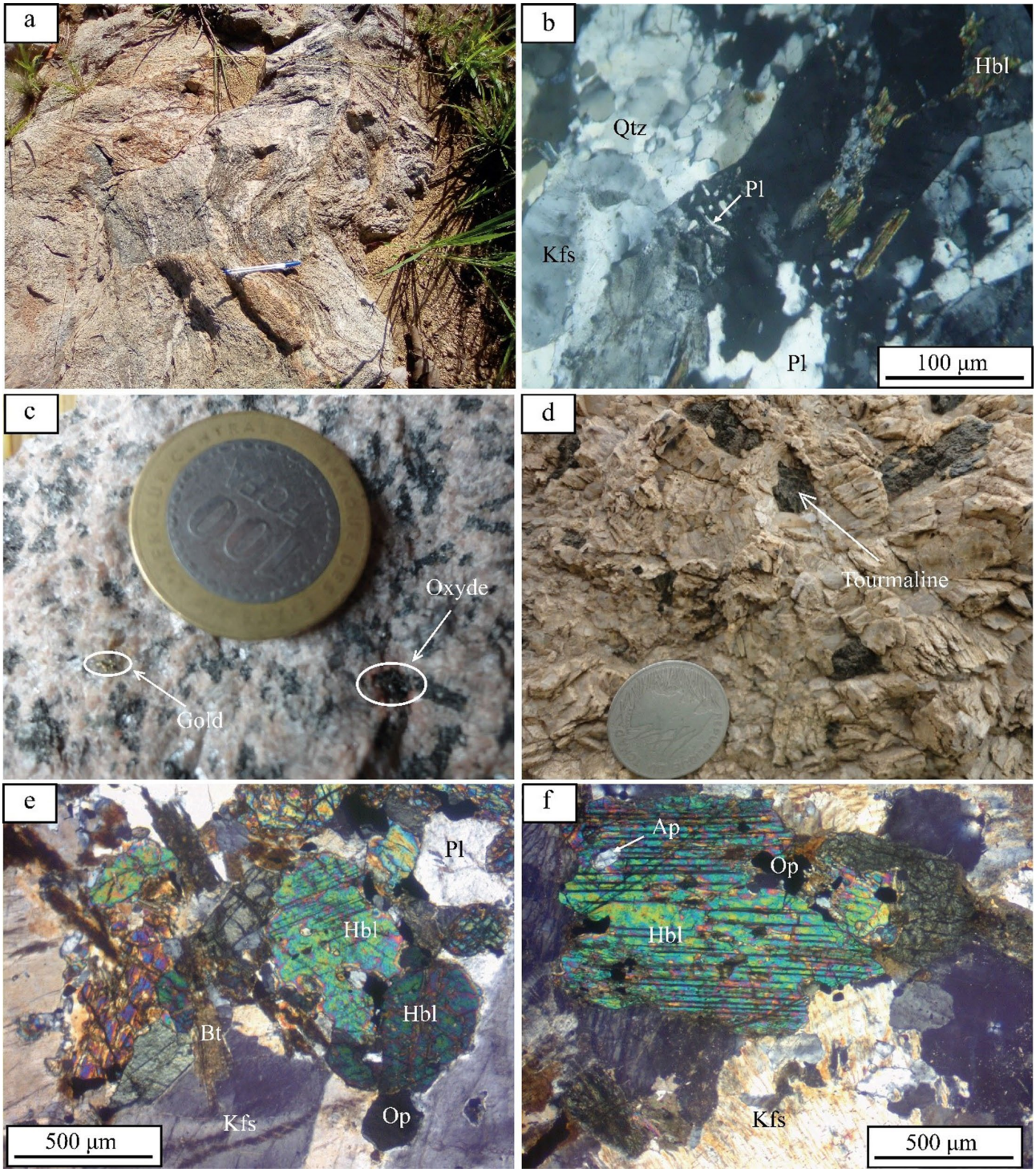

Figure 11. Photographs and microphotographs of gneisses and syenites from the study area (a) gneiss outcrop; (b) micrographs (under crossed polarized light) of gneisses; (c) a sample of syenite exhibiting a gold nugget and oxides; (d) a pegmatite vein containing tourmaline; (e) (f) microphotograph of syenite showing amphibole, plagioclase, oxides, and biotite.

ilmenite series and are therefore ilmenite syenites (**Figure 12(a)**). The Rb vs. K2O diagram by [83] shows that the syenites of Baïbokoum belong to the non-specialized syenites, suggesting that they are generally sterile (**Figure 12(b)**).

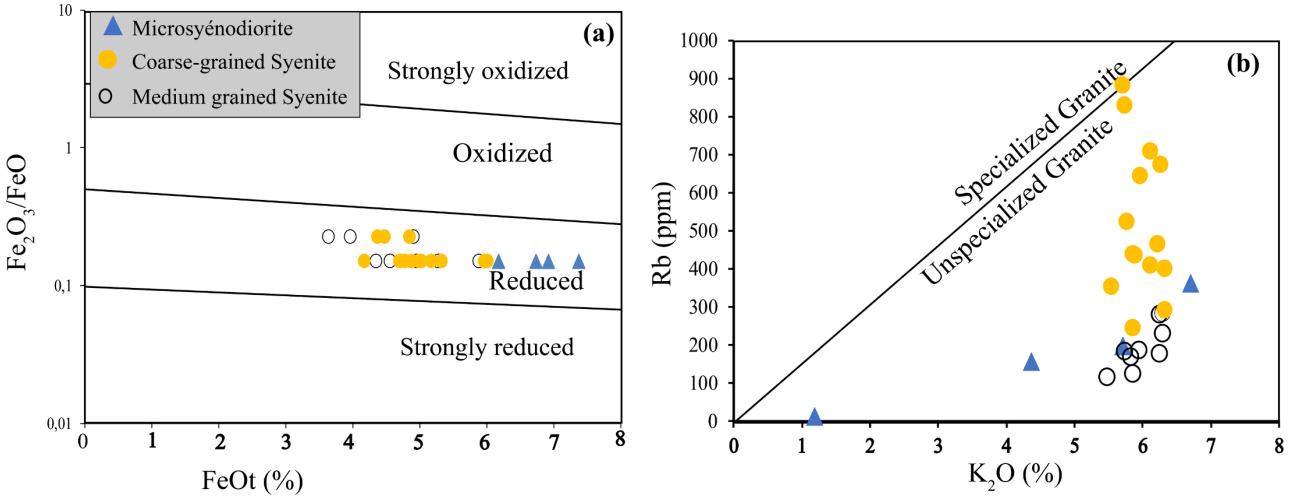

Figure 12. Metallogenic potential of the plutonic rocks of Baïbokoum: (a) Fe_2O_3/FeO vs. FeOt diagram by [82]; (b) Rb vs. K2O diagram by [83].

The syenites of Baïbokoum show significant concentrations of certain REEs (Ce = 204, Pr = 27.3, Nd = 104, Yb = 3.57, Er = 3.74, Dy = 5.57, Gd = 10.15 ppm). These syenites show an increase in their ΣREE and their (La/Lu)N ratios (**Figure 13(a)**), reflecting a process of normal magmatic differentiation. The variation in rare earth content in the magmatic rocks of Baïbokoum is similar to the variation in rare earth concentrations in syenitic rocks solidifying through normal magmatic differentiation without magmatic fluid (**Figure 13(a)**). LREE concentrations increase from the first to the last episodes of magmatic formation in Baïbokoum. This characteristic trend can be explained by certain processes [84]: (i) one possibility is the crystallization and accumulation of LREE-rich minerals such as allanite, apatite, and monazite from residual magma in the early stages of the formation of the Baïbokoum syenites.

REE concentrations increase in syenites and vary from 109.49 to 524.02 ppm, because REEs very often concentrate in the magmatic fluid as incompatible elements during the fractional crystallization process. A negative correlation between SiO_2 and ΣHREE contents in the analyzed syenites (**Figure 13(b)**) suggests that HREE are depleted by magma fractionation. The Baïbokoum syenites are slightly depleted in HREE (ΣHREE = 10.16 - 22 ppm) compared to the HREE-enriched syenites of the REE deposits in SW Japan (ΣHREE = 10 - 100 ppm; [85] Ishihara and Murakami, 2006) and in southern China (ΣHREE = 38 - 79 ppm; [86]).

The negative correlation observed between SiO_2 content and ΣLREE in the Baïbokoum syenites shows that LREE content is relatively high between 54% and 66% SiO_2 (**Figure 13(c)**). Since LREE very often represent the majority of REE concentrations, the ΣLREE (**Figure 13(c)**) and ΣREE (**Figure 13(d)**) diagrams as a function of SiO_2 content show a similar distribution pattern for the samples. This result suggests that REE-rich minerals crystallized early in the highly fractionated magma.

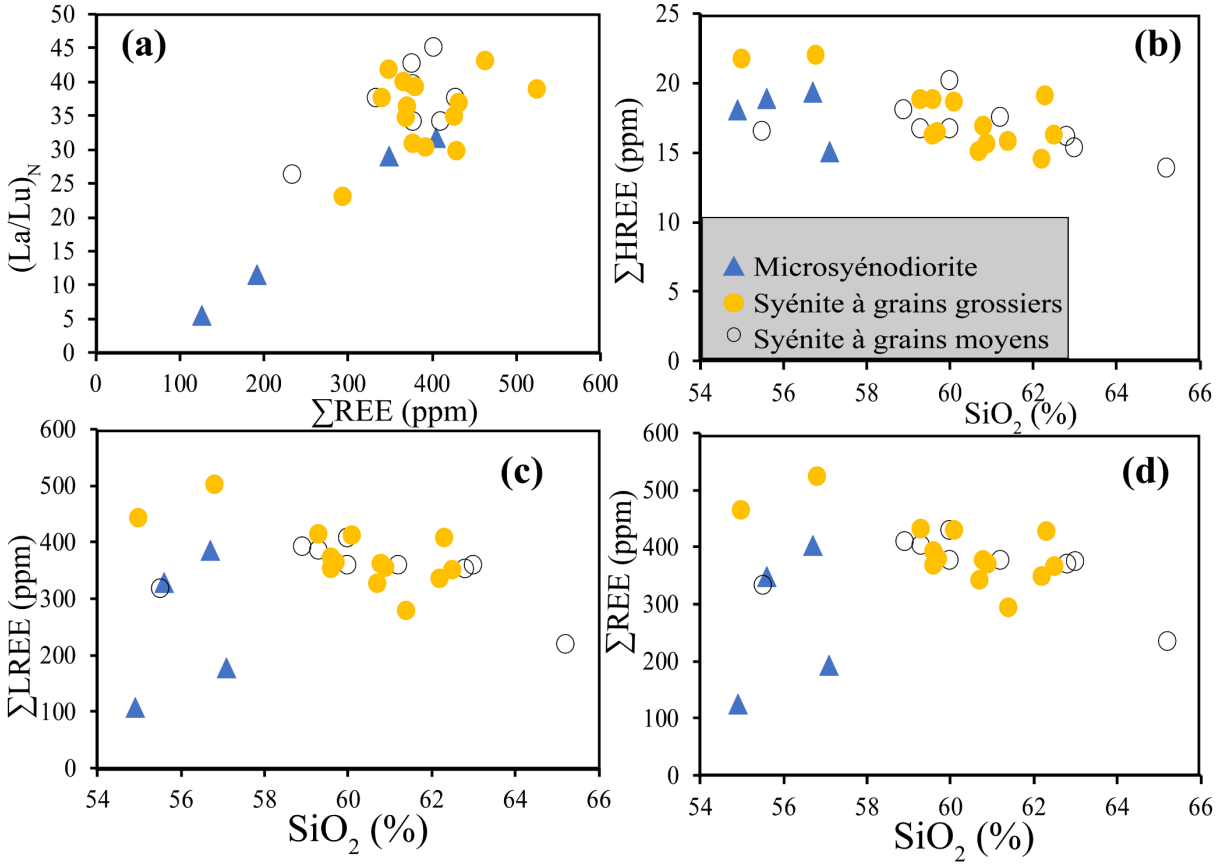

Figure 13. Discrimination of rare earth mineralization in the Baïbokoum syenites: (a) Diagrams showing the relationship between (La/Lu)N ratios and ΣREE (ppm); (b) ΣHREE (ppm); (c) ΣLREE (ppm); (d) ΣREE (ppm) vs. SiO_2 (%) in Baïbokoum syenites.

The REE concentrations in Baïbokoum syenites, ranging from 109.49 ppm to 524.02 ppm, are significantly higher than those found in syenitic rocks in Laos (35 - 339 ppm; [87] and syenites in ion-adsorption-type REE deposits (130 - 350 ppm: [86] [88]. Although syenitic rocks in ion-adsorption-type REE deposits are distinctly depleted in HREE (LREE/HREE = 5.97 - 23.54) compared to other REE deposits, the others are enriched in LREE (LREE/HREE = 6.7 - 18.7) as reported by [89] and [88]. All Baïbokoum syenites are depleted in HREE and enriched in LREE, showing mostly high LREE/HREE ratios ranging from 5.97 to 23.54 (mostly > 10).

7. Analysis of Histograms and Box Plots

Geochemical anomalies are detected by establishing thresholds, which define the upper and lower limits of normal fluctuation for a specific set of data. Data within the threshold range are considered normal, while those that exceed or fall below these thresholds are perceived as anomalies. The bars on the left side of the histogram (**Figure 14**) illustrate samples with a maximum concentration of a certain trace metal that is closer to or above the upper limit, thus indicating positive anomalies within the sample population. Bar charts often illustrate an asymmetrical

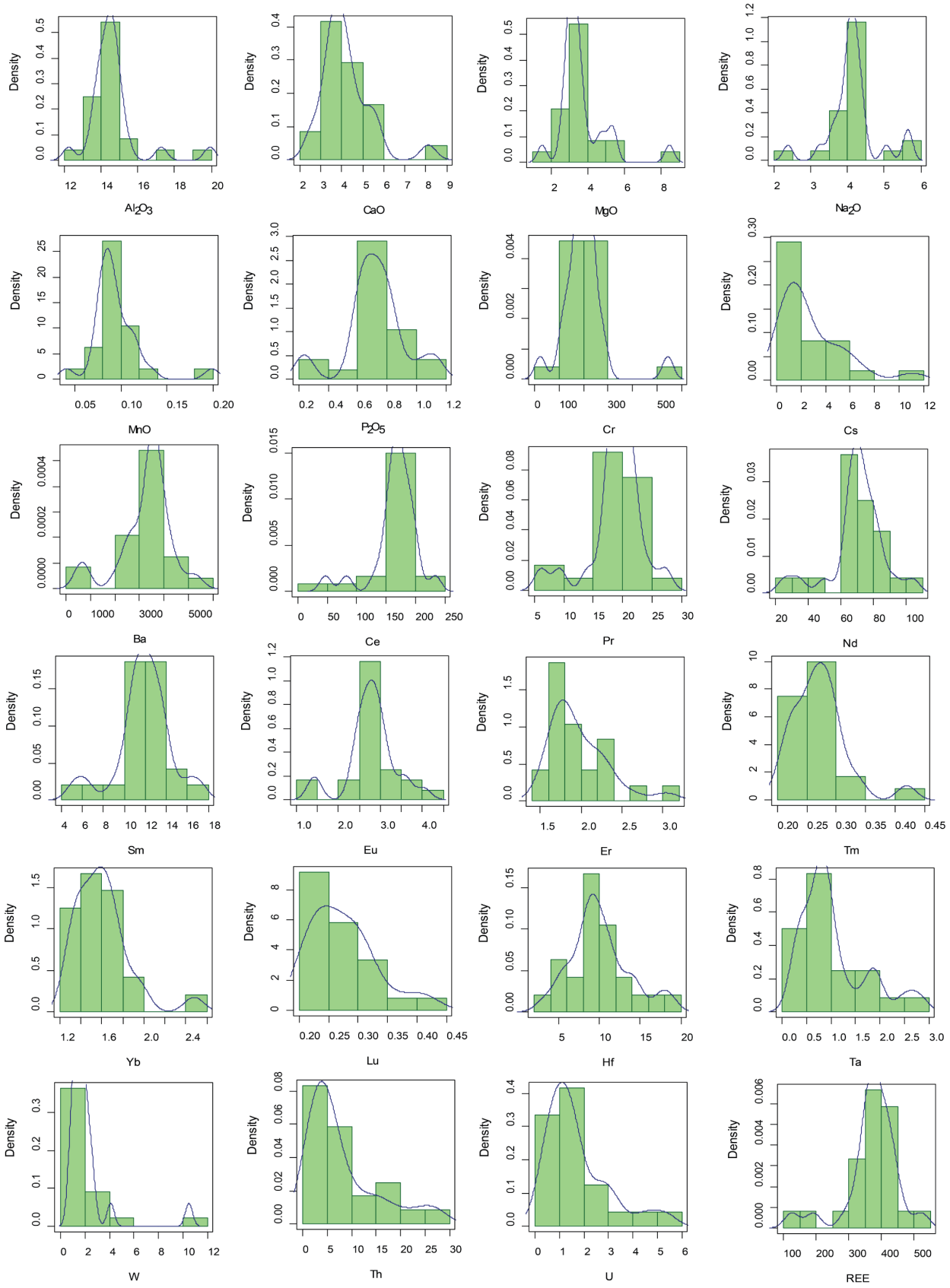

Figure 14. Histograms showing the distribution of mineralization indices in syenites and microsyenodiorites in the study area.

distribution of mineral components in rocks (**Figure 14**). However, the majority of samples have multiple data points, visible through the marked spacing between the histogram bars (concentration in two populations), a common phenomenon in the distribution of geochemical data [90] [91].

Several data distributions indicate fractional crystallization or magmatic fluid, a change in composition, and the influence of hydrothermal alteration [90] [91].

The box plots are represented on the left, while outliers are found on the right, indicating that the concentrations of these respective elements/metals in syenites and microsyenodiorites are low and clustered around the lower percentile (**Figure 15**). Based on the calculated threshold, the concentrations of elements in the samples (**Table 4**) show anomalies in certain elements/metals according to the threshold

Table 4. Statistics for element concentrations (in ppm) in plutonic rocks in the study area. Crustal values are from [92]. *[93].

Element	Sample	Mean	Min	25%	50%	75%	Max	Threshold	Crustal Abundance
Al_2O_3	24	14.66	12.23	13.90	14.45	14.80	19.94	16.16	15.40
CaO	24	4.19	2.49	3.52	4.03	4.57	8.12	6.15	5.60
MgO	24	3.68	1.52	3.02	3.36	3.72	8.46	4.78	3.80
Na_2O	24	4.14	2.38	3.94	4.10	4.30	5.65	4.84	3.30
MnO	24	0.09	0.04	0.08	0.09	0.10	0.20	0.14	0.10
P_2O_5	24	0.72	0.23	0.62	0.71	0.81	1.14	1.08	0.13*
Cr	24	204	23	166	197	228	545	321	126
Cs	24	2.8	0.18	0.9	1.72	4.12	11.1	8.95	3.4
Ba	24	3280	587	2815	3500	3700	5280	5027.5	584
Ce	24	165.2	46.8	155.8	169.5	183.5	234	225.05	60
Pr	24	18.89	6.1	17.79	19.1	21.05	27.3	25.94	6.7
Nd	24	70.2	25.6	66.6	70.2	79	104	97.6	27
Sm	24	11.84	5.24	10.87	12.05	13.16	17.15	16.595	5.3
Eu	24	2.78	1.4	2.52	2.77	3.01	4.04	3.745	1.3
Er	24	1.97	1.54	1.74	1.86	2.17	3.05	2.815	2.1
Tm	24	0.27	0.2	0.24	0.27	0.29	0.42	0.365	0.3
Yb	24	1.6	1.3	1.43	1.57	1.69	2.48	2.08	2
Lu	24	0.27	0.2	0.23	0.26	0.3	0.42	0.405	0.35
Hf	24	10.07	3.36	8.23	9.32	11.44	18.55	16.255	4.9
Ta	24	1	0.3	0.6	0.8	1.2	2.8	2.1	1.1
W	22	2.1	0.8	1.3	1.7	2.1	10.5	3.3	1
Th	24	7.95	0.75	3.1	5.33	10.52	27.5	21.65	8.5
U	24	1.71	0.21	0.86	1.38	2.12	5.32	4.01	1.7
REE	24	371.03	125.77	348.58	377.15	413.76	524.02	511.53	144.3

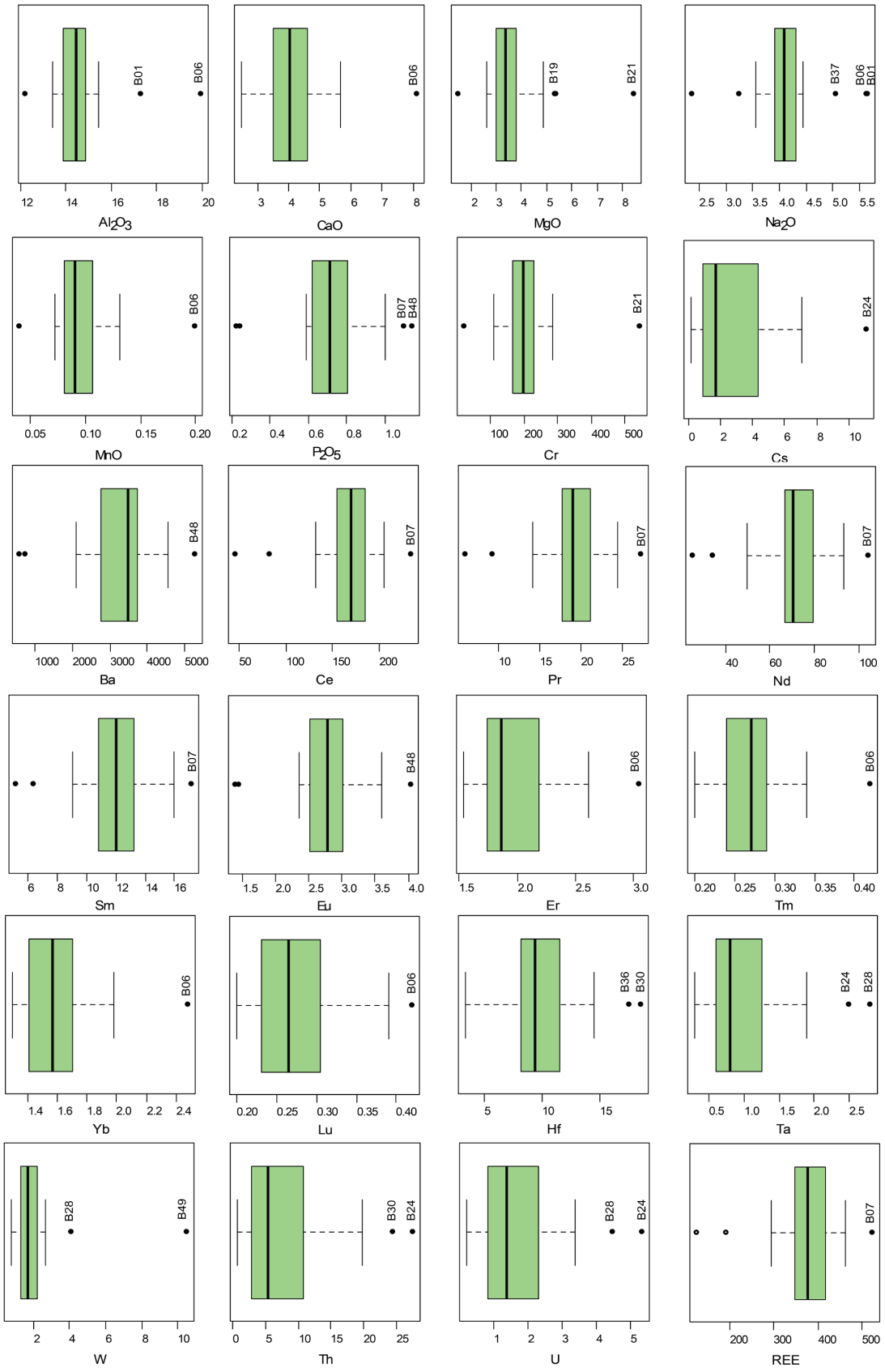

Figure 15. Box plots of the variation in the concentration of metals/useful elements in samples of syenites and microsyenodiorites.

calculated for each of them, compared to the maximum concentrations analyzed. According to the statistical table, the syenites and microsyenodiorites in the study area show enrichment in Al_2O_3, Fe_2O_3, MgO, CaO, Na_2O, MnO, P_2O_5, V, Cr, W, Zr, Nb, Cs, Ba, Y, Hf, Ta, Th, U, and REE, resulting in the formation of positive geochemical anomalies in these elements (**Figure 15**). Furthermore, concentrations of TiO_2, K_2O, Sr, and HREE are lower than their respective thresholds and would indicate depletion resulting in the formation of negative geochemical anomalies in these elements in the syenites and microsyenodiorites of the study area (**Figure 15**). In general, the results of the statistical analysis show eight (08) mineralization indices in the study area, namely: (i) Al_2O_3-MnO-V-Cr in microsyenodiorite; (ii) Fe_2O_3-CaO in microsyenodiorite; (iii) Y in syenodiorite; (iv) MgO in microsyenodiorite, medium-grained syenite, and coarse-grained syenite; (v) Na_2O in microsyenodiorite and coarse-grained syenite; (vi) P_2O_5-W-Ba-REE in coarse-grained syenite; (vii) Cs in medium-grained syenite; (viii) Zr-Nb-Hf-Ta-Th-U in medium-grained syenite and coarse-grained syenite.

8. Discussion

8.1. Contribution of Geospatial Data and Field Observations

The ability to map lithology and minerals was greatly improved by integrating FCC, PCA, MNF, BR, CEM, and SAM using Landsat 9 OLI data. PCA and MNF offered dimensional reduction and noise suppression, which improved feature extraction, while FCC and BR offered visual and semi-quantitative improvements. Accurate mineral identification and supervised lithological and mineral classification were made possible by SAM and CEM respectively.

[94] suggests that FCC pictures may enhance understanding of lithological units and hydrothermally altered rocks on a local or regional scale [24] [25] [35]. Furthermore, some mineral groups and minerals in changed lithologies exhibit unique electromagnetic absorption capabilities [35] [25].

PCA reduced data redundancy by concentrating spectral variability into the first few components [24] [25]. [95] explains that the sign and magnitude of eigenvectors are dictated by the spectral properties of minerals and rocks that contribute to statistical variance in each PC. **Table 1** shows that PC1, PC2, and PC3 have substantial eigenvector loadings for bands 7, 5, and 3.

MNF transformed the OLI data to maximize signal while minimizing noise [25]. Helped extract subtle spectral differences within homogeneous lithologies. MNF images were particularly effective in improving the signal for low-reflectance units such as syenites and shale.

Suppressing topographic effects and enhancing subtle mineralogical differences [24] [25]. These BR helped delineate alteration halos and weathered rock units, aiding early mineral exploration targeting. All hydrothermal minerals display unique spectral signatures on multi-spectral remote sensing systems, determined by their texture and mineralogy [24] [96]. Focusing on the research area's hydrothermally changed regions and rock units allowed for the discovery of alteration

mineral deposits, such as iron oxides, ferrous, and clay minerals.

According to the USGS spectral analysis database, the analyzed minerals show higher reflectance and absorption values than it usually does. The CEM method used OLI bands 753 to solve common problems with adaptive beam formation in signal processing [35] [96] [97] to detect the aforementioned minerals using the USGS spectral library.

We used the SAM method on the FCC 753 to sort the lithological units we found in the study area (**Figure 8**). We used an angle radian of 0.1 for correlation and high exactness [25] [35] [96] [98] with a value of 100% and a Kappa coefficient of 1.0 (**Table 3**). This shows that the method works well and is accurate for lithological classification.

Processing the panchromatic band (B8) brought out important lineaments that help us figure out how hydrothermal minerals move through the study area.

Using GIS tool to combine FCC, PCA, MNF, BR, CEM and SAM data led to the creation of a synthesis geological-mineralization map of the study area (**Figure 16**).

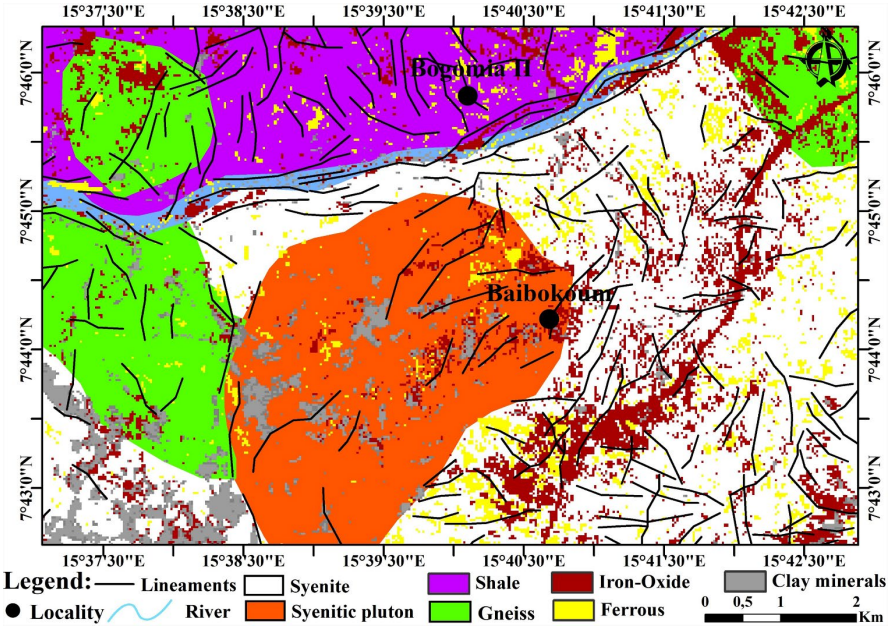

Figure 16. Baïbokoum synthesis litho-mineral map.

Because of the limited surface exposures and subtle mineralogical contrasts found in Precambrian terrains, this multi-technique approach proved particularly effective. Better discrimination over older sensors was further supported by the use of Landsat 9's enhanced radiometric resolution.

8.2. Contribution of Statistical Analysis and Metallogenic Significance

In the mineral exploration sector, attention is generally focused on positive anomalies, assuming that mineral-rich regions and their subsequent leaching have am-

plified the concentration of elements beyond the usual standards of the Earth's crust. However, negative anomalies can also be important, particularly when they illustrate a decrease in certain components/metals during the modification of surrounding rocks that accompanies the mineralization process [7] [8] [99].

The selected elements, although they have different chemical properties, behave similarly during fractional crystallization. According to [100], chalcopyrite is the main element in copper ore, while zinc ore consists mainly of ferromagnetic silicates. Copper deposits usually form either in volcanic arc zones above subduction zones or in post-collisional magmatism that forms at the end of the subduction process [101] [102]. This is the case in the Baïbokoum region, which is located within the Pan-African chain in Central Africa. In both environments, the distinction between productive and barren rocks with respect to selected major and rare earth elements is regularly based on the overall geochemistry of the rocks [31] [103]-[106]. According to [92], granitoids containing mineralization of the selected elements have Clarke values between 0.3 and 144.3. In the samples analyzed, Clarke values range from 0.36 to 511.53.

Vegetation poses a considerable challenge for mineral remote sensing, mainly in the visible and near-infrared range, as it camouflages the underlying rock while introducing its own spectral signature. Precise mineral signatures (such as those of clay alteration, which stimulates the growth of certain types of vegetation) can only be identified indirectly. MNF and PCA methods can help distinguish between certain spectral variations related to noise and vegetation, but they cannot eliminate them entirely. Erosion, by exposing new rocks or altered areas, can be beneficial because it makes the surface more accessible for remote sensing [17] [25] [32]. However, excessive erosion can complicate the detection of the initial spectral signatures of the source rock or primary mineralization, as it has the potential to reveal deeper alteration strata or amalgamate various minerals.

The orientations of the detected lineaments (E-W, NNE-SSE to NW-SE, and NE-SW) in the studied region are due to shear zones, which are frequently permeable and can serve as channels for the movement of metal-laden hydrothermal fluids [38]. It is possible that these fluids transported and deposited mineralization along these gold, copper, or polymetallic veins. Tourmalinization, for example, may be common along these zones, indicating high-temperature hydrothermal processes.

9. Conclusion

The study demonstrates the integration of Landsat 9 OLI data with fieldwork, petrography and structural analysis to discriminate mineral-bearing geological formations. Remote sensing techniques such as RGB, PCA, BR, CEM, MNF and SAM combinations were applied to detect significant mineral-bearing rock units. The RGB, BR, PCA and MNF methods proved relevant and effective for the exploration of rock units, while the specialized BR, CEM and LSU techniques proved more effective and significant for the detection of iron oxide and hydroxyl miner-

als. The SAM technique proved to be the most effective classification method for mapping lithological units and mineral deposits. According to the field survey and microscopic analysis, the host rocks are syenites, syenodiorites and gneisses. The occurrence of strongly predominant lineaments (E-W, NNE-SSE to NW-SE, and NE-SW) is considered highly potential zone for concentrating iron oxide and hydroxyl minerals. The results of this study demonstrated that the combined application of digital mapping techniques to Landsat 9 data, combined with field and laboratory analysis, provides useful geological information that can be an essential tool and database for mineral exploration in the Baïbokoum region. Statistical geochemical analysis suggests that the Baïbokoum syenites are "reduced", "non-specialized", and have high concentrations of Al_2O_3, Fe_2O_3, MgO, CaO, Na_2O_3, MnO, P_2O_5, V, Cr, W, Zr, Nb, Cs, Ba, Y, Hf, Ta, Th, U and REE. The summary map indicates that the rocks show variability in terms of the abundance and distribution of metal-bearing minerals, including indications of target areas with high iron oxide potential. The most crucial priority areas are located in the eastern, southern, and northeastern sectors.

Acknowledgements

We would like to express our gratitude to the editor and anonymous reviewers for their critical comments on the manuscript.

Authors' Contributions

Baïssemia Ronang Gustave: Conceptualization, Methodology, Software, Writing—original version. **Mbaguedjé Diondoh:** Conceptualization, Methodology, Software, Writing—original version. **Ndjerossem Nénadji Félix:** Conceptualization, Methodology, Software, Copywriting—original version. **Safianou Ousmanou:** Conceptualization, Methodology, Software, Copywriting—original version. **Abdoulaye Nourene Souleymane:** Conceptualization, Methodology, Software, Copywriting—original version. **Gountié Dedzo Merlin:** Data curation, Writing—original version. **Kwékam Maurice:** Supervision.

Conflicts of Interest

The authors declare no conflicts of interest regarding the publication of this paper.

References

[1] Hegab, M.A. (2021) Remote Sensing and Gamma-Ray Spectrometry Based Gold Related Alteration Zones Detection: Case Study (Um Balad Area), North Eastern Desert, Egypt. *Pure and Applied Geophysics*, **178**, 3909-3931. https://doi.org/10.1007/s00024-021-02865-1

[2] Harraz, H.Z. (1999) Wall Rock Alteration, Atud Gold Mine, Eastern Desert, Egypt: Processes and $P\ T\ X_{CO2}$ Conditions of Metasomatism. *Journal of African Earth Sciences*, **28**, 527-551. https://doi.org/10.1016/s0899-5362(99)00031-7

[3] Abrams, M.J., Brown, D., Lepley, L. and Sadowski, R. (1983) Remote Sensing for

Porphyry Copper Deposits in Southern Arizona. *Economic Geology*, **78**, 591-604. https://doi.org/10.2113/gsecongeo.78.4.591

[4] Mbassa, B.J., Njonfang, E., Grégoire, M., Itiga, Z., Kamgang, P., Benoit, M., *et al.* (2018) Evaluation of the Mineralizing Potential of the Mbengwi Plutonics, Northwestern Cameroon, Central Africa. *Arabian Journal of Geosciences*, **11**, 656-669. https://doi.org/10.1007/s12517-018-4018-0

[5] Fozing, E.M., Kwékam, M., Tetsopgang, S., Njanko, T., Chako-Tchamabé, B., Kouémo, J.T., *et al.* (2021) The Mineralization Potential of the I-Type Granites from Misajé Pluton (NW-Cameroon): AMS and Geochemical Constraints. *Solid Earth Sciences*, **6**, 283-296. https://doi.org/10.1016/j.sesci.2021.06.002

[6] Yannah, M., Fodoué, Y., Kwékam, M., Mbassa, B.J., Tifang, J.A., Kagou, A.D., *et al.* (2022) Geochemical Evaluation of Mineralization Potential of the Somie-Ntem Area within the Tikar Plain, Cameroon: Implication on Petrogenesis. *Acta Geochimica*, **41**, 861-886. https://doi.org/10.1007/s11631-022-00552-z

[7] Chen, J., Zhao, Z., Yang, Y., Li, C., Yin, Y., Zhao, X., *et al.* (2024) Metallogenic Prediction Based on Fractal Theory and Machine Learning in Duobaoshan Area, Heilongjiang Province. *Ore Geology Reviews*, **168**, Article 106030. https://doi.org/10.1016/j.oregeorev.2024.106030

[8] Zhao, Z., Zhao, X., Yin, Y., Li, C., Yang, Y. and Wang, Y. (2024) Identification of Geochemical Anomalies Based on RPCA and Multifractal Theory: A Case Study of the Sidaowanzi Area, Chifeng, Inner Mongolia. *ACS Omega*, **9**, 24998-25013. https://doi.org/10.1021/acsomega.4c02078

[9] Baïssemia Ronang, G., Gountié Dedzo, M., Tcheumenak Kouémo, J., Klamadji, M.N., Mbaguedjé, D. and Kwékam, M. (2025) Petrography and Geochemical Characterization of the Baïbokoum Syenitic Pluton (Southern Chad): Implication for the Magma Genesis. *Acta Geochimica*, **44**, 420-439. https://doi.org/10.1007/s11631-024-00733-y

[10] Seguem, N., Alexandre, G.A., Klötzli, U., Kepnamou, A.D. and Emmanuel, E.G. (2014) Petrography and Geochemistry of Precambrian Basement Straddling the Cameroon-Chad Border: The Touboro Baïbokoum Area. *International Journal of Geosciences*, **5**, 418-431. https://doi.org/10.4236/ijg.2014.54040

[11] Seguem, N., Diondoh, M., Kepnamou, A.D., Mama, N., Sami, M., Alexandre, G.A., *et al.* (2022) Petrography and Geochemistry of Baïbokoum-Touboro-Ngaoundaye Granitoids on the Chad-Cameroon-RCA Borders (Adamawa-Yade Domain). *Open Journal of Geology*, **12**, 136-155. https://doi.org/10.4236/ojg.2022.122007

[12] Zhang, N., Zhou, K. and Du, X. (2017) Application of Fuzzy Logic and Fuzzy AHP to Mineral Prospectivity Mapping of Porphyry and Hydrothermal Vein Copper Deposits in the Dananhu-Tousuquan Island Arc, Xinjiang, NW China. *Journal of African Earth Sciences*, **128**, 84-96. https://doi.org/10.1016/j.jafrearsci.2016.12.011

[13] Hegab, M.A.E., Mousa, S.E., Salem, S.M. and Moustafa, M.S. (2023) ASTER and Aerospectrometric Data Analysis for Gold Exploration: Case Study at Um Balad Area, North Eastern Desert, Egypt. In: Gad, A.A., Elfiky, D., Negm, A. and Elbeih, S., Eds., *Springer Proceedings in Earth and Environmental Sciences*, Springer Nature, 49-54. https://doi.org/10.1007/978-3-031-40447-4_6

[14] Akinlalu, A.A., Afolabi, D.O. and Sanusi, S.O. (2024) Knowledge-Driven Fuzzy AHP Model for Orogenic Gold Prospecting in a Typical Schist Belt Environment: A Mineral System Approach. *Earth Systems and Environment*, **8**, 221-263. https://doi.org/10.1007/s41748-024-00382-4

[15] Ousmanou, S., Fodoue, Y., Wadjou, J.W., Kepnamou, A.D., Fozing, E.M., Kwékam, M., *et al.* (2024) Fuzzy-Logic Technique for Gold Mineralization Prospecting Using

Landsat 9 OLI Processing and Fieldwork Data in the Bibemi Goldfield, North Cameroon. *Heliyon*, **10**, e23334. https://doi.org/10.1016/j.heliyon.2023.e23334

[16] Sanusi, S.O., Olaniyan, O., Afolabi, D.O. and Olayanju, G.M. (2024) Mapping of Orogenic Gold Mineralization Potential in the Kushaka Schist Belt, Northcentral Nigeria: Insights from Point Pattern, Kernel Density, Staged-Factor, and Fuzzy AHP Modeling Techniques. *Earth Systems and Environment*, **9**, 135-184. https://doi.org/10.1007/s41748-024-00427-8

[17] Pour, A.B., Hashim, M. and van Genderen, J. (2013) Detection of Hydrothermal Alteration Zones in a Tropical Region Using Satellite Remote Sensing Data: Bau Goldfield, Sarawak, Malaysia. *Ore Geology Reviews*, **54**, 181-196. https://doi.org/10.1016/j.oregeorev.2013.03.010

[18] Pour, A.B., Hashim, M. and Marghany, M. (2014) Exploration of Gold Mineralization in a Tropical Region Using Earth Observing-1 (EO1) and JERS-1 SAR Data: A Case Study from Bau Gold Field, Sarawak, Malaysia. *Arabian Journal of Geosciences*, **7**, 2393-2406. https://doi.org/10.1007/s12517-013-0969-3

[19] Takodjou Wambo, J.D., Pour, A.B., Ganno, S., Asimow, P.D., Zoheir, B., Salles, R.d.R., *et al.* (2020) Identifying High Potential Zones of Gold Mineralization in a Sub-Tropical Region Using Landsat-8 and ASTER Remote Sensing Data: A Case Study of the Ngoura-Colomines Goldfield, Eastern Cameroon. *Ore Geology Reviews*, **122**, Article 103530. https://doi.org/10.1016/j.oregeorev.2020.103530

[20] Abdelkareem, M. and El-Baz, F. (2018) Characterizing Hydrothermal Alteration Zones in Hamama Area in the Central Eastern Desert of Egypt by Remotely Sensed Data. *Geocarto International*, **33**, 1307-1325. https://doi.org/10.1080/10106049.2017.1325410

[21] Shi, K., Chang, Z., Chen, Z., Wu, J. and Yu, B. (2020) Identifying and Evaluating Poverty Using Multisource Remote Sensing and Point of Interest (POI) Data: A Case Study of Chongqing, China. *Journal of Cleaner Production*, **255**, Article 120245. https://doi.org/10.1016/j.jclepro.2020.120245

[22] Alarifi, S.S., Abdelkareem, M., Abdalla, F., Abdelsadek, I.S., Gahlan, H., Al-Saleh, A.M., *et al.* (2022) Fusion of Multispectral Remote-Sensing Data through GIS-Based Overlay Method for Revealing Potential Areas of Hydrothermal Mineral Resources. *Minerals*, **12**, Article 1577. https://doi.org/10.3390/min12121577

[23] Zhou, G., Zhang, H., Xu, C., Zhou, X., Liu, Z., Zhao, D., *et al.* (2023) A Real-Time Data Acquisition System for Single-Band Bathymetric Lidar. *IEEE Transactions on Geoscience and Remote Sensing*, **61**, 1-21. https://doi.org/10.1109/tgrs.2023.3282624

[24] Safianou, O, Fozing, E.M., Kwékam, M., Yaya, F. and Leprince, D.A.J. (2023) Application of Remote Sensing Techniques in Lithological and Mineral Exploration: Discrimination of Granitoids Bearing Iron and Corundum Deposits in Southeastern Banyo, Adamawa Region Cameroon. *Earth Science Informatics*, **16**, 259-285.

[25] Ousmanou, S., Martial, F.E., Jules, T.K., Ludovic, A.M., Agnès Blandine, K.T., Sufinatu, A., *et al.* (2024) Mapping and Discrimination of the Mineralization Potential in Granitoids from Banyo Area (Adamawa, Cameroon), Using Landsat 9 OLI, ASTER Images and Field Observations. *Geosystems and Geoenvironment*, **3**, Article 100239. https://doi.org/10.1016/j.geogeo.2023.100239

[26] Zhang, X., Pazner, M. and Duke, N. (2007) Lithologic and Mineral Information Extraction for Gold Exploration Using ASTER Data in the South Chocolate Mountains (California). *ISPRS Journal of Photogrammetry and Remote Sensing*, **62**, 271-282. https://doi.org/10.1016/j.isprsjprs.2007.04.004

[27] Sanusi, S.O. and Amigun, J.O. (2020) Logistic-Based Translation of Orogenic Gold

Forming Processes into Mappable Exploration Criteria for Fuzzy Logic Mineral Exploration Targeting in the Kushaka Schist Belt, North-Central Nigeria. *Natural Resources Research*, **29**, 3505-3526. https://doi.org/10.1007/s11053-020-09689-1

[28] Fozing, E.M., Tcheumenak Kouémo, J., Sâga, S., Chako Tchamabé, B., Ousmanou, S., Foka Koagne, S., *et al.* (2024) Integrating Geospatial Data and Multi-Criteria Analysis for Mapping and Evaluating the Mineralization Potential of the Dschang Pluton (Western Cameroon). *Earth Science Informatics*, **17**, 5625-5653. https://doi.org/10.1007/s12145-024-01475-4

[29] Yao, Y., Murphy, P.J. and Robb, L.J. (2001) Fluid Characteristics of Granitoid-Hosted Gold Deposits in the Birimian Terrane of Ghana: A Fluid Inclusion Microthermometric and Raman Spectroscopic Study. *Economic Geology*, **96**, 1611-1643. https://doi.org/10.2113/gsecongeo.96.7.1611

[30] Allibone, A., Hayden, P., Cameron, G. and Duku, F. (2004) Paleoproterozoic Gold Deposits Hosted by Albite- and Carbonate-Altered Tonalite in the Chirano District, Ghana, West Africa. *Economic Geology*, **99**, 479-497. https://doi.org/10.2113/gsecongeo.99.3.479

[31] Sun, X., Li, R., Sun, H., Olin, P.H., Santosh, M., Fu, B., *et al.* (2024) Genesis of Pb-Zn-Ag-Sb Mineralization in the Tethys Himalaya, China: Early Magmatic-Hydrothermal Pb-Zn(-Ag) Mineralization Overprinted by Sb-Rich Fluids. *Mineralium Deposita*, **59**, 1275-1293. https://doi.org/10.1007/s00126-024-01264-5

[32] Traore, M., Takodjou Wambo, J.D., Ndepete, C.P., Tekin, S., Pour, A.B. and Muslim, A.M. (2020) Lithological and Alteration Mineral Mapping for Alluvial Gold Exploration in the South East of Birao Area, Central African Republic Using Landsat-8 Operational Land Imager (OLI) Data. *Journal of African Earth Sciences*, **170**, Article 103933. https://doi.org/10.1016/j.jafrearsci.2020.103933

[33] Cerny, P. and Ercit, T.S. (2005) The Classification of Granitic Pegmatites Revisited. *The Canadian Mineralogist*, **43**, 2005-2026. https://doi.org/10.2113/gscanmin.43.6.2005

[34] Taylor, S.R. and McLennan, S.M. (1985) The Continental Crust: Its Composition and Evolution. Blackwell Scientific Publication, 312.

[35] Ghodsi, M.R., Boomeri, M., Bagheri, S., Lentz, D. and Ishiyama, D. (2016) Metallogeny and Mineralization Potential of the Bazman Granitoids, SE Iran. *Resource Geology*, **66**, 286-302. https://doi.org/10.1111/rge.12102

[36] Mbaguedjé, D. (2015) Métallogénie de l'or et de l'uranium dans le cadre de la croissance et de la différenciation de la croûte au néoprotérozoïque: Exemple du massif du mayo-kebbi (Tchad) dans la ceinture orogénique d'afrique centrale. Thèse de Doctorat en Géosciences, Université de Lorraine, 269 p.

[37] Tchameni, R., Doumnang, J.C., Deudibaye, M. and Branquet, Y. (2013) On the Occurrence of Gold Mineralization in the Pala Neoproterozoic Formations, South-Western Chad. *Journal of African Earth Sciences*, **84**, 36-46. https://doi.org/10.1016/j.jafrearsci.2013.03.002

[38] Malik, M.H., NgonNgon, G.F., Vishiti, A., Mayer, A.A., Isseini, M., Djerossem, F., *et al.* (2024) Petrography and Mineral Microchemical Signature of Lode Gold Mineralization in Goz-Beida, Southern Ouaddaï Massif, Eastern Chad. *Arabian Journal of Geosciences*, **17**, Article No. 207. https://doi.org/10.1007/s12517-024-12011-5

[39] Meert, J.G. and Lieberman, B.S. (2007) The Neoproterozoic Assembly of Gondwana and Its Relationship to the Ediacaran-Cambrian Radiation. *Gondwana Research*, **14**, 5-21. https://doi.org/10.1016/j.gr.2007.06.007

[40] Abdelsalam, M.G., Gao, S.S. and Liégeois, J. (2011) Upper Mantle Structure of the

Saharan Metacraton. *Journal of African Earth Sciences*, **60**, 328-336. https://doi.org/10.1016/j.jafrearsci.2011.03.009

[41] Poidevin, J.L. (1991) Les ceintures de roches vertes de la république centrafricaine. contribution à la connaissance du précambrien du nord du craton du congo. Doctoratd'Etat, Université Blaise Pascal.

[42] Rolin, P. (1995) La zone de décrochements panafricains des oubanguides en république centrafricaine. *Comptes Rendu de L'académie des Sciences de Paris*, **320**, 63-69.

[43] Toteu, S.F., Van Schmus, W.R., Penaye, J. and Michard, A. (2001) New U-Pb and Sm-Nd Data from North-Central Cameroon and Its Bearing on the Pre-Pan African History of Central Africa. *Precambrian Research*, **108**, 45-73. https://doi.org/10.1016/s0301-9268(00)00149-2

[44] Toteu, S.F., Penaye, J. and Djomani, Y.P. (2004) Geodynamic Evolution of the Pan-African Belt in Central Africa with Special Reference to Cameroon. *Canadian Journal of Earth Sciences*, **41**, 73-85. https://doi.org/10.1139/e03-079

[45] Toteu, S.F., Penaye, J., Deloule, E., Van Schmus, W.R. and Tchameni, R. (2006) Diachronous Evolution of Volcano-Sedimentary Basins North of the Congo Craton: Insights from U-Pb Ion Microprobe Dating of Zircons from the Poli, Lom and Yaoundé Groups (Cameroon). *Journal of African Earth Sciences*, **44**, 428-442. https://doi.org/10.1016/j.jafrearsci.2005.11.011

[46] Ngako, V., Affaton, P., Nnange, J.M. and Njanko, T. (2003) Pan-African Tectonic Evolution in Central and Southern Cameroon: Transpression and Transtension during Sinistral Shear Movements. *Journal of African Earth Sciences*, **36**, 207-214. https://doi.org/10.1016/s0899-5362(03)00023-x

[47] Njonfang, E., Ngako, V., Kwekam, M. and Affaton, P. (2006) Les orthogneiss calco-alcalins de foumban-bankim: Témoins d'une zone interne de marge active panafricaine en cisaillement. *Comptes Rendus. Géoscience*, **338**, 606-616. https://doi.org/10.1016/j.crte.2006.03.016

[48] Tchakounté, J., Eglinger, A., Toteu, S.F., Zeh, A., Nkoumbou, C., Mvondo-Ondoa, J., *et al.* (2017) The Adamawa-Yadé Domain, a Piece of Archaean Crust in the Neoproterozoic Central African Orogenic Belt (Bafia Area, Cameroon). *Precambrian Research*, **299**, 210-229. https://doi.org/10.1016/j.precamres.2017.07.001

[49] Abdelsalam, M.G., Liégeois, J. and Stern, R.J. (2002) The Saharan Metacraton. *Journal of African Earth Sciences*, **34**, 119-136. https://doi.org/10.1016/s0899-5362(02)00013-1

[50] Nzenti, J.P., Barbey, P., Macaudiere, J. and Soba, D. (1988) Origin and Evolution of the Late Precambrian High-Grade Yaounde Gneisses (Cameroon). *Precambrian Research*, **38**, 91-109. https://doi.org/10.1016/0301-9268(88)90086-1

[51] van Schmus, W.R., Oliveira, E.P., da Silva Filho, A.F., Toteu, S.F., Penaye, J. and Guimarães, I.P. (2008) Proterozoic Links between the Borborema Province, NE Brazil, and the Central African Fold Belt. *Geological Society, London, Special Publications*, **294**, 69-99. https://doi.org/10.1144/sp294.5

[52] Wacrenier, P. (1958) Carte géologique provisoire du borkou-ennedi-tibesti. Direction de Mine et Géologie.

[53] El Makkrouf, A.A. (1988) Tectonic Interpretation of Jabal Eghei Area and Its Regional Application to Tibesti Orogenic Belt, South Central Libya (S.P.L.A.J.). *Journal of African Earth Sciences* (*and the Middle East*), **7**, 945-967. https://doi.org/10.1016/0899-5362(88)90009-7

[54] Suayah, I.B., Miller, J.S., Miller, B.V., Bayer, T.M. and Rogers, J.J.W. (2006) Tectonic Significance of Late Neoproterozoic Granites from the Tibesti Massif in Southern Libya Inferred from Sr and Nd Isotopes and U-Pb Zircon Data. *Journal of African Earth Sciences*, **44**, 561-570. https://doi.org/10.1016/j.jafrearsci.2005.11.020

[55] Kasser, M.Y. (1995) Evolution précambrienne de la région du Mayo Kebbi (Tchad). Un segment de la Chaîne Panafricaine. Doctorat de 3ème Cycle, Muséum d'Histoire Naturelle de Paris, 217 p.

[56] Djerossem, N.F. (2018) Croissance et remobilisation crustales au pan-africain dans le Sud du massif du ouaddaï (Tchad oriental). Thèse de Doctorat en Géosciences Environnement Toulouse, Université Toulouse-3 Paul Sabatier, 302 p.

[57] Djerossem, F., Berger, J., Vanderhaeghe, O., Isseini, M., Ganne, J. and Zeh, A. (2020) Neoproterozoic Magmatic Evolution of the Southern Ouaddaï Massif (Chad). *BSGF-Earth Sciences Bulletin*, **191**, Article 34. https://doi.org/10.1051/bsgf/2020032

[58] Liégeois, J.P. (1992) Mesures des isotopes du Sr en vue de détermination d'âges des roches magmatiques du Sud du Tchad (région Baïbokoum, Léré-Figuil). 10.

[59] Shellnutt, J., Pham, N.H.T., Yeh, MW. and Lee, T.Y. (2020) Two Series of Ediacaran Collision-Related Granites in the Guéra Massif, South-Central Chad: Tectonomagmatic Constraints on the Terminal Collision of the Eastern Central African Orogenic Belt. *Precambrian Research*, **347**, Article 105823.

[60] de Wit, M.J., Bowring, S., Buchwaldt, R., Dudas, F.Ö., MacPhee, D., Tagne-Kamga, G., *et al.* (2021) Geochemical Reconnaissance of the Guéra and Ouaddaï Massifs in Chad: Evolution of Proterozoic Crust in the Central Sahara Shield. *South African Journal of Geology*, **124**, 353-382. https://doi.org/10.25131/sajg.124.0048

[61] Mbaïtoudji, M.M. (1982) Géotraverse au tchad, au sud du quatorzième parallèle nord. DRGM.

[62] Mbaitoudji, M.M. (1984) Lois de répartition, hypothèse de pronostics et méthodologie de la recherche des gisements de minéraux utiles solides dans le territoire de la République du Tchad. Publication CIFEG, 14 p.

[63] Black, R. (1992) Mission géologique au Tchad du 14/1 au 08/02/1992. PNUD/DRGM, 15 p.

[64] Kusnir, I. and Moutaye, H.A. (1997) Ressources minérales du Tchad: Une revue. *Journal of African Earth Sciences*, **24**, 549-562. https://doi.org/10.1016/s0899-5362(97)00080-8

[65] Mbaïtoudji, M.M. (1982) Lois de répartition, hypothèses de pronostics et méthodologie de la recherche des gisements de minéraux utiles solides dans le territoire de la république du tchad. Institut de Prospection géologique, Moscou (URSS).

[66] Penaye, J., Kröner, A., Toteu, S.F., Van Schmus, W.R. and Doumnang, J. (2006) Evolution of the Mayo Kebbi Region as Revealed by Zircon Dating: An Early (ca. 740ma) Pan-African Magmatic Arc in Southwestern Chad. *Journal of African Earth Sciences*, **44**, 530-542. https://doi.org/10.1016/j.jafrearsci.2005.11.018

[67] Pouclet, A., Vidal, M., Doumnang, J.-C., Vicat, J.-P. and Tchameni, R. (2006) Neoproterozoic Crustal Evolution in Southern Chad: Pan-African Ocean Basin Closing, Arc Accretion and Late- to Post-Orogenic Granitic Intrusion. *Journal of African Earth Sciences*, **44**, 543-560. https://doi.org/10.1016/j.jafrearsci.2005.11.019

[68] Isseini, M. (2011) Croissance et différenciation crustales au Néoprotérozoïque: Exemple du domaine panafricain du mayo-kebbi au sud-ouest du tchad. Thèse de Doctorat Université Henri Poincaré, 339 p.

[69] Isseini, M., André-Mayer, A., Vanderhaeghe, O., Barbey, P. and Deloule, E. (2012) A-

type Granites from the Pan-African Orogenic Belt in South-Western Chad Constrained Using Geochemistry, Sr-Nd Isotopes and U-Pb Geochronology. *Lithos*, **153**, 39-52. https://doi.org/10.1016/j.lithos.2012.07.014

[70] Doumnang, J.C. (2006) La géologie des formations néoprotérozoïques du mayo-kebbi (S-W du Tchad). Thèse de Doctorat, Université d'Orléans, 206 p.

[71] Kusnir, I. (1995) Géologie, ressources minérales et ressources en eau du Tchad. Centre National d'Appui à la Recherche.

[72] Diontar, M., Doumnang, J.C., Kwékam, M., Al-hadj Hamid, Z., Kagou Dongmo, A., Efon Awoum, J., *et al.* (2020) Petrogenesis of Magnesian High-K Granitoids from Bitkine (Centrechad Massif): Major and Trace Elements Constraints. *European Journal of Environment and Earth Sciences*, **1**, 1-5. https://doi.org/10.24018/ejgeo.2020.1.5.78

[73] Mbaihoudou, D., Maurice, K., Martial, F.E., Armand, K.D. and Jules, T.K. (2020) Petrology and Geochemical Characteristic of Granitoids from Guéra Massif in the Central Part of Chad: An Example of Mixing Magmas. *Earth Science Research*, **9**, 66-84. https://doi.org/10.5539/esr.v9n2p66

[74] Njanko, T., Nédélec, A. and Affaton, P. (2006) Synkinematic High-K Calc-Alkaline Plutons Associated with the Pan-African Central Cameroon Shear Zone (W-Tibati Area): Petrology and Geodynamic Significance. *Journal of African Earth Sciences*, **44**, 494-510. https://doi.org/10.1016/j.jafrearsci.2005.11.016

[75] Mapoka, H.Y., Danguene, P.E., Nzenti, J.P., Biandja, J, Kankeu, B. and Sheo, E.S. (2011) Major Structural Features and the Tectonic Evolution of the Bossangoa-Bossembele Basement, Northwestern Central African Republic. *The Open Geology Journal*, **5**, 21-32. https://doi.org/10.2174/1874262901105010021

[76] Bernstein, L.S., Jin, X., Gregor, B. and Adler-Golden, S.M. (2012) Quick Atmospheric Correction Code: Algorithm Description and Recent Upgrades. *Optical Engineering*, **51**, Article 111719. https://doi.org/10.1117/1.oe.51.11.111719

[77] Budd, A.R., Wyborn, L.A.I and Bastrakova, I.V. (2001) The Metallogenic Potential of Australian Proterozoic Granites. Geosciences Australian Recherche.

[78] Wyrborn, A.I.L. (2002) Ganites and Copper-Gold Metallogenesis in the Australian Proterozoic. *Proceedings of Geosciences Australia*, 1-51.

[79] Dhana, R. (2008) I-, M-, A- and S-Type Granitoids: Their Attributes and Mineralization, with Indian Examples. *Journal of Economic Geology and Georesource Management*, **5**, 1-23.

[80] Janoušek, V., Farrow, C.M. and Erban, V. (2006) Interpretation of Whole-Rock Geochemical Data in Igneous Geochemistry: Introducing Geochemical Data Toolkit (GCDkit). *Journal of Petrology*, **47**, 1255-1259. https://doi.org/10.1093/petrology/egl013

[81] Yusta, I., Velasco, F. and Herrero, J. (1998) Anomaly Threshold Estimation and Data Normalization Using EDA Statistics: Application to Lithogeochemical Exploration in Lower Cretaceous Zn-Pb Carbonate-Hosted Deposits, Northern Spain. *Applied Geochemistry*, **13**, 421-439. https://doi.org/10.1016/s0883-2927(97)00095-4

[82] Champion, D.C. and Heinemann, M.A. (1994) Igneous Rocks of North Queensland: 1/500 000 Map and Explanatory Notes. Australian Geological Survey Organisation, 11-82.

[83] Tuach, J., Davenport, P.H., Dickson, W.L. and Strong, D.F. (1986) Geochemical Trends in the Ackley Granite, Southeast Newfoundland: Their Relevance to Magmatic-Metallogenic Processes in High-Silica Granitoid Systems. *Canadian Journal of*

Earth Sciences, **23**, 747-765. https://doi.org/10.1139/e86-077

[84] Ishiyama, D., Miyata, M., Shibata, S., Satoh, H., Mizuta, T., Fukuyama, M., *et al.* (2011) Geochemical Characteristics of Miocene Fe-Cu-Pb-Zn Granitoids Associated Mineralization in the Chichibu Skarn Deposit (Central Japan): Evidence for Magmatic Fluids Generation Coexisting with Granitic Melt. *Geological Society, London, Special Publications*, **350**, 69-88. https://doi.org/10.1144/sp350.5

[85] Ishihara, S. and Murakami, H. (2006) Fractionated Ilmenite-Series Granites in Southwest Japan: Source Magma for Ree-Sn-W Mineralizations. *Resource Geology*, **56**, 245-256. https://doi.org/10.1111/j.1751-3928.2006.tb00282.x

[86] Wu, C., Huang, D. and Guo, Z. (1990) REE Geochemistry in the Weathered Crust of Granites, Longnan Area, Jiangxi Province. *Acta Geologica Sinica-English Edition*, **3**, 193-209. https://doi.org/10.1111/j.1755-6724.1990.mp3002006.x

[87] Sanematsu, K., Murakami, H., Watanabe, Y., Duangsurigna, S. and Siphandone, V. (2009) Enrichment of Rare Earth Elements (REE) in Granitic Rocks and Their Weathered Crusts in Central and Southern Laos. *Bulletin of the Geological Survey of Japan*, **60**, 527-558. https://doi.org/10.9795/bullgsj.60.527

[88] Bao, Z. and Zhao, Z. (2008) Geochemistry of Mineralization with Exchangeable REY in the Weathering Crusts of Granitic Rocks in South China. *Ore Geology Reviews*, **33**, 519-535. https://doi.org/10.1016/j.oregeorev.2007.03.005

[89] Wu, C., Yuan, Z. and Bai, G. (1996) Rare Earth Deposits in China. In: Jones, A.P., Wall, F. and Williams, C.T., Eds., *Rare Earth Minerals: Chemistry Origin and Ore Deposits*, *The Mineralogical Society Series* 7, Chapman et Hall, 281-310.

[90] Reimann, C. and Filzmoser, P. (2000) Normal and Lognormal Data Distribution in Geochemistry: Death of a Myth. Consequences for the Statistical Treatment of Geochemical and Environmental Data. *Environmental Geology*, **39**, 1001-1014. https://doi.org/10.1007/s002549900081

[91] Reimann, C., Filzmoser, P. and Garrett, R.G. (2005) Background and Threshold: Critical Comparison of Methods of Determination. *Science of The Total Environment*, **346**, 1-16. https://doi.org/10.1016/j.scitotenv.2004.11.023

[92] Hans Wedepohl, K. (1995) The Composition of the Continental Crust. *Geochimica et Cosmochimica Acta*, **59**, 1217-1232. https://doi.org/10.1016/0016-7037(95)00038-2

[93] Rudnick, R.L. and Gao, S. (2003) Composition of the Continental Crust. *Treatise on Geochemistry*, **3**, 1-64. https://doi.org/10.1016/b0-08-043751-6/03016-4

[94] Pour, A.B. and Hashim, M. (2015) Hydrothermal Alteration Mapping from Landsat-8 Data, Sar Cheshmeh Copper Mining District, South-Eastern Islamic Republic of Iran. *Journal of Taibah University for Science*, **9**, 155-166. https://doi.org/10.1016/j.jtusci.2014.11.008

[95] Loughlin, W.P. (1991) Principal Components Analysis for Alteration Mapping. *Photogrammetric Engineering and Remote Sensing*, **57**, 1163-1169.

[96] Madeleine, N.M., Martial, F.E., Ousmanou, S., Ludovic, A.M., Belmien, S.Y.R. and Sâga, S. (2025) Mapping and Discrimination of the Mineralization Potential in the Bonako Area (Central Cameroon Domain): Insights from Landsat 9 OLI Data, GIS Fuzzy Modeling Techniques and Field Observations. *Geosystems and Geoenvironment*, **4**, Article ID: 100347. https://doi.org/10.1016/j.geogeo.2024.100347

[97] Mohamed, R., Tamen, J., Ousmanou, S., Yangouo, F.K. and Nkouathio, D. (2024) Lithological Discrimination Based on Landsat-9 OLI Sensor and Field Observation Data: The Bana An-Orogenic Volcano-Plutonic Ring Complex, West Cameroon Line. *Heliyon*, **10**, e36806. https://doi.org/10.1016/j.heliyon.2024.e36806

[98] Richard, J. (1999) Remote Sensing Digital Image Analysis. Springer-Verlag, 240.

[99] McQueen, K.G. (2008) Identify in Geochemical Anomalies. CRC Leme, 1-7.

[100] Bahajroy, M. and Taki, S. (2014) Study of the Mineralization Potential of the Intrusives around Valis (Taromiran). *Earth Sciences Research Journal*, **18**, 123-129. https://doi.org/10.15446/esrj.v18n2.44799

[101] Sillitoe, R.H. (2010) Porphyry Copper Systems. *Economic Geology*, **105**, 3-41. https://doi.org/10.2113/gsecongeo.105.1.3

[102] Richards, J.P. (2011) Magmatic to Hydrothermal Metal Fluxes in Convergent and Collided Margins. *Ore Geology Reviews*, **40**, 1-26. https://doi.org/10.1016/j.oregeorev.2011.05.006

[103] Baldwin, J.A. and Pearce, J.A. (1982) Discrimination of Productive and Nonproductive Porphyritic Intrusions in the Chilean Andes. *Economic Geology*, **77**, 664-674. https://doi.org/10.2113/gsecongeo.77.3.664

[104] Asadi, S., Moore, F. and Zarasvandi, A. (2014) Discriminating Productive and Barren Porphyry Copper Deposits in the Southeastern Part of the Central Iranian Volcano-Plutonic Belt, Kerman Region, Iran: A Review. *Earth-Science Reviews*, **138**, 25-46. https://doi.org/10.1016/j.earscirev.2014.08.001

[105] Zarasvandi, A., Rezaei, M., Sadeghi, M., Lentz, D., Adelpour, M. and Pourkaseb, H. (2015) Rare Earth Element Signatures of Economic and Sub-Economic Porphyry Copper Systems in Urumieh-Dokhtar Magmatic Arc (UDMA), Iran. *Ore Geology Reviews*, **70**, 407-423. https://doi.org/10.1016/j.oregeorev.2015.01.010

[106] Runsheng, H., Yan, Z., Wenlong, Q., Tianzhu, D., Mingzhi, W. and Feng, W. (2023) Geology and Geochemistry of Zn-Pb(-Ge-Ag) Deposits in the Sichuan-Yunnan-Guizhou Triangle Area, China: A Review and a New Type. *Frontiers in Earth Science*, **11**, Article ID: 1136397. https://doi.org/10.3389/feart.2023.1136397